Cylicins are a structural component of the sperm calyx being indispensable for male fertility in mice and human

Simon Schneider[1,2,†], Andjela Kovacevic[1,†], Michelle Mayer[1,3], Ann-Kristin Dicke[4], Lena Arévalo[1], Sophie A. Koser[4], Jan N. Hansen[5], Samuel Young[6], Christoph Brenker[6], Sabine Kliesch[6], Dagmar Wachten[5], Gregor Kirfel[7], Timo Strünker[6], Frank Tüttelmann[4] and Hubert Schorle[1,*]

[1] Institute of Pathology, Department of Developmental Pathology, Medical Faculty, University of Bonn, 53127 Bonn, Germany

[2] Bonn Technology Campus, Core Facility "Gene-Editing", Medical Faculty, University of Bonn, 53127 Bonn, Germany

[3] Present address: Life and Medical Sciences Institute, Department for Immunology and Environment, University of Bonn, 53115 Bonn, Germany

[4] Institute of Reproductive Genetics, University of Münster, 48149 Münster, Germany

[5] Institute of Innate Immunity, Biophysical Imaging, Medical Faculty, University of Bonn, 53127 Bonn, Germany

[6] Centre of Reproductive Medicine and Andrology, University Hospital Münster, University of Münster, 48149 Münster, Germany

[7] Institute for Cell Biology, University of Bonn, 53121 Bonn, Germany

[*]correspondence: Hubert.Schorle@ukbonn.de

† contributed equally

Abstract

Cylicins are testis-specific proteins, which are exclusively expressed during spermiogenesis. In mice and humans, two Cylicins, the gonosomal X-linked Cylicin 1 (*Cylc1/CYLC1*) and the autosomal Cylicin 2 (*Cylc2/CYLC2)* genes have been identified. Cylicins are cytoskeletal proteins with an overall positive charge due to lysine-rich repeats. While Cylicins have been localized in the acrosomal region of round spermatids, they resemble a major component of the calyx within the perinuclear theca at the posterior part of mature sperm nuclei. However, the role of Cylicins during spermiogenesis has not yet been investigated. Here, we applied CRISPR/Cas9-mediated gene-editing in zygotes to establish *Cylc1*- and *Cylc2*-deficient mouse lines as a model to study the function of these proteins. *Cylc1* deficiency resulted in male subfertility, whereas *Cylc2*$^{-/-}$, *Cylc1*$^{-/Y}$ *Cylc2*$^{+/-}$, and *Cylc1*$^{-/Y}$ *Cylc2*$^{-/-}$ males were infertile. Phenotypical characterization revealed that loss of Cylicins prevents proper calyx assembly during spermiogenesis. This results in decreased epididymal sperm counts, impaired shedding of excess cytoplasm, and severe structural malformations, ultimately resulting in impaired sperm motility. Furthermore, exome sequencing identified an infertile man with a hemizygous variant in *CYLC1* and a heterozygous variant in *CYLC2*, displaying morphological abnormalities of the sperm including the absence of the acrosome. Thus, our study highlights the relevance and

importance of Cylicins for spermiogenic remodeling and male fertility in human and mouse, and provides the basis for further studies on unraveling the complex molecular interactions between perinuclear theca proteins required during spermiogenesis.

Keywords: *Cylc1*, *Cylc2*, Cylicin, male infertility, subfertility, sperm, calyx, perinuclear theca, cytoskeleton, manchette, motility, CRISPR, gene-editing

Introduction

The differentiation of round spermatids into sperm during spermiogenesis is a highly organized and spatiotemporally controlled process taking place in the seminiferous epithelium of the testis. Cellular and morphological remodeling involves DNA hypercondensation, establishment of a species-specific head morphology, removal of excess cytoplasm as well as formation of accessory structures like acrosome and flagellum. These structural changes depend on a highly efficient protein trafficking machinery and a unique sperm cytoskeleton [1]. One essential cytoskeletal element is the perinuclear theca (PT), which surrounds the sperm nucleus, except for the caudal edge, at the implantation site of the flagellum. The PT is supposed to serve as a structural scaffold for the sperm nucleus and resembles a rigid cytosolic protein layer, which is resistant to non-ionic detergents and high salt buffer extractions [2, 3]. The PT has been subdivided into a subacrosomal and postacrosomal part based on its localization, function, composition, and developmental origin. The subacrosomal part of the PT develops early during spermiogenesis, simultaneously with the formation of the acrosome. It is supposed to emerge from acrosomal vesicles, and presents as a thin cytosolic protein layer between the inner acrosomal membrane and the nuclear envelope [4, 5]. The postacrosomal part of the PT, also known as the sperm calyx, originates from cytosolic proteins that are transported via the manchette and assembled during sperm head elongation [4]. It is located in between the nuclear envelope and the sperm plasma membrane.

Proteomic analyses using murine and bovine PT extracts revealed 500-800 different proteins, highlighting its high molecular complexity [6, 7]. Apart from cytoskeletal proteins, signaling molecules and several *de novo* synthesized core histones were identified. They are proposed to be essential for sperm-egg interaction and chromatin remodeling of the male pronucleus at early post-fertilization stages [8, 9, 4, 10, 11]. Many structural proteins of the PT are testis-specific and uniquely expressed in the PT, including Calicin (*Ccin*) [12, 2, 13], Cylicin 1 (*Cylc1*) and Cylicin 2 (*Cylc2*) [2, 14, 15], actin-capping proteins CPβ3 and CPα3 [16–18] as well as actin-related proteins Arp-T1 and Arp-T2 [19]. Despite being characterized on molecular level, their function remains largely elusive.

72 Both, *Ccin* and Cylicins are highly basic proteins with a predominant localization in the calyx of
73 mature sperm [14, 15, 12]. In most species, two Cylicin genes, *Cylc1* and *Cylc2*, have been identified
74 (Figure 1-supplement 1). They are characterized by repetitive lysine-lysine-aspartic acid (KKD) and
75 lysine-lysine-glutamic acid (KKE) peptide motifs, resulting in an isoelectric point (IEP) > pH 10 [14, 15].
76 Repeating units of up to 41 amino acids in the central part of the molecules stand out by a predicted
77 tendency to form individual short α-helices [14]. Mammalian Cylicins exhibit similar protein and domain
78 characteristics, but CYLC2 has a much shorter amino-terminal portion than CYLC1 (Figure 1 -
79 supplement 1). While the *CYLC2/Cylc2* gene is encoded on autosomes, the human and murine
80 *CYLC1/Cylc1* gene is encoded on the X-chromosome, resulting in hemizygosity in males. Further, in
81 bovine, Cylc2 serves as actin-binding protein of the sperm perinuclear cytoskeleton [20]. Cylicins seem
82 to be cytoskeletal regulators and required for proper sperm head architecture.

83 In this study, we report the CRISPR/Cas9-mediated generation and characterization of *Cylc1-*, *Cylc2-*,
84 and *Cylc1/2*-deficient mice, demonstrating that Cylicins are indispensable for male fertility and play a
85 key function in the formation of the sperm calyx. We show that Cylicins are required for the
86 maintenance of the PT integrity during spermiogenesis and in mature sperm. Their deficiency results
87 in morphological defects of the sperm head, acrosome, and mid-piece. Our analyses revealed that
88 *Cylicin* genes are evolutionary conserved in rodents and primates. Furthermore, we identified Cylicin
89 variants in an infertile man, demonstrating the conserved role of Cylicins in regulating male
90 infertility.

91

92 **Results**

93 **Cylicins are indispensable for male fertility in mice**

94 Cylicins were first discovered and characterized in the early nineties due to their subcellular
95 localization a role in sperm head architecture was postulated [2, 14, 15], . To address the question of the
96 role of Cylicins during spermiogenesis, we used CRISPR/Cas9-mediated gene-editing to generate
97 *Cylc1-* and *Cylc2*-deficient mouse models. First, for *Cylc1*, a pair of sgRNAs targeting exon 5 was
98 designed, and a mouse line with a frameshift inducing deletion of 1.585 kb, accounting for 85% of the
99 *Cylc1* coding sequence, was established (Fig. 1 A). Next, two guide RNAs targeting exon 4/5 of the
100 *Cylc2* gene were applied to establish a *Cylc2*-deficient mouse line with a 1.145 kb frameshift inducing
101 deletion (Fig. 1 A). In both lines, the majority of predicted functional domains with repetitive, lysine-
102 lysine-aspartic acid (KKD) and lysine-lysine-glutamic acid (KKE) peptide motifs were depleted.
103 Deletion was confirmed by PCR-based genotyping (Fig. 1 B).

104 Fertility testing of *Cylc1*$^{-/y}$ males revealed significantly reduced pregnancy rates (16 %) and mean
105 litter size (2.2) (Fig. 1 C). *Cylc2*$^{-/-}$ males were infertile, while *Cylc2*$^{+/-}$ males showed no significant

106 difference in fertility parameters compared to wildtype mice (Fig. 1 C). Additionally, established
107 mouse lines were intercrossed to generate *Cylc1*$^{-/y}$ *Cylc2*$^{+/-}$ and *Cylc1*$^{-/y}$ *Cylc2*$^{-/-}$ males. Of note, *Cylc1*$^{-/y}$
108 *Cylc2*$^{+/-}$, and *Cylc1*$^{-/y}$ *Cylc2*$^{-/-}$ males were infertile (Fig. 1 C). This indicates that loss of *Cylc1* alone is
109 partially tolerated, as suggested by subfertility of *Cylc1*$^{-/y}$ males, whereas the additional loss of one
110 *Cylc2* allele renders male mice infertile. Taken together, the results suggest, that two functional
111 Cylicin alleles are required for male fertility.

112 qRT PCR confirmed the absence of *Cylc1* and/or *Cylc2* transcripts in Cylicin-deficient animals (Fig. 1
113 D). In *Cylc2*$^{+/-}$ animals expression of *Cylc2* was reduced by 50 %. Neither loss of *Cylc1* nor *Cylc2*
114 resulted in upregulation of *Cylc2* or *Cylc1*, respectively.

115 Next, due to the lack of commercial antisera, polyclonal antibodies against murine CYLC1 and CYLC2
116 were raised to visualize the localization of Cylicins during spermiogenesis. Specificity of antibodies
117 was proven by immunohistochemical stainings (IHC), showing a specific signal in testis sections only,
118 but not in any other organ tested (Figure 1 - supplement 2). Immunofluorescence staining of
119 wildtype testicular tissue showed presence of both, CYLC1 and CYLC2 from the round spermatid
120 stage onward (Fig. 1 E). The signal was first detectable in the subacrosomal region as a cap-like
121 structure, lining the developing acrosome (Fig. 1 E-F, Figure 1 – supplement 3). As the spermatids
122 elongate, CYLC1 and CYLC2 move across the PT towards the caudal part of the cell (Figure 1 –
123 supplement 4). At later steps of spermiogenesis, the localization in the subacrosomal part of the PT
124 faded, while it intensified in the postacrosomal calyx region (Fig. 1 E-F). Of note, the localization of
125 CYLC1 and CYLC2 in the calyx of mature sperm has been reported in bovine and human. The
126 generated antibodies did not stain testicular tissue and mature sperm of *Cylc1*- and *Cylc2*-deficient
127 males, except for a very weak unspecific background staining in the lumen of seminiferous tubules
128 and the residual bodies of testicular sperm (Fig. 1 E). Additionally, Western Blot analyses confirmed
129 the absence of CYLC1 and CYLC2 in cytoskeletal protein fractions of the respective knockout (Fig. 1
130 G), thereby demonstrating i) specificity of the antibodies and ii) validating the gene knockout. Of
131 note, the CYLC1 antibody detects a double band at 40-45 KDa. This is smaller than the predicted size
132 of 74 KDa as, but both bands were absent in Cylc1$^{-/y}$. Similarly, the CYLC2 Antibody detected a double
133 band at 38-40 KDa instead of 66 KDa. Again, both bands were absent in *Cylc2*$^{-/-}$. Next, Mass
134 spectrometry analysis of cytoskeletal protein fraction of mature spermatozoa was performed
135 detecting both proteins in WT but not in the respective knockout samples (Figure 1 – supplement 5;
136 Figure 1 – supplement 6).

137

138 **Sperm morphology is severely altered in Cylicin-deficient mice**

139 Next, spermiogenesis of Cylicin-deficient males was analyzed in detail. Gross testicular morphology
140 as well as testicular weight were not significantly altered (Fig. 2 A, B). The testicular morphology
141 appeared unaltered, with all stages of spermatogenesis being detectable in hematoxylin and eosin
142 (HE) stained testicular sections (Figure 2 – supplement 1). However, a strong decline in cauda
143 epididymal sperm counts was observed in all Cylicin-deficient males. For *Cylc1*$^{-/y}$ and *Cylc2*$^{+/-}$ males, a
144 moderate reduction of 40-47% was determined, whereas *Cylc2*$^{-/-}$ and *Cylc1*$^{-/y}$ *Cylc2*$^{+/-}$ displayed an
145 approx. 65% reduction in epididymal sperm counts compared to wildtype mice (Fig. 2 C). In *Cylc1*$^{-/y}$
146 *Cylc2*$^{-/-}$ males, spermiogenesis was most impaired, as indicated by an 85% reduction of the sperm
147 count (Fig. 2 C). Eosin-Nigrosin staining revealed that the viability of epididymal sperm from all
148 genotypes was not severely affected (Fig. 2 D, Figure 2 – supplement 2). However, viability of *Cylc2*$^{-/-}$
149 and *Cylc1*$^{-/y}$ *Cylc2*$^{-/-}$ sperm was significantly reduced by approx. 15% compared to wildtype sperm.
150 (Fig. 2 D).

151 Next, we used brightfield microscopy to evaluate the effects of Cylicin deficiency on sperm
152 morphology. Above all, coiling of the sperm tails and kinked sperm heads were observed in *Cylc2*$^{-/-}$
153 and *Cylc1*$^{-/y}$ *Cylc2*$^{-/-}$ males (Fig. 2 E). To confirm this, we used PNA-FITC lectin immunofluorescence
154 staining to analyze acrosome localization in mature sperm, MITOred to visualize mitochondria in the
155 flagellum and DAPI to stain the nucleus (Fig. 2 F). Loss of *Cylc1* alone caused malformations of the
156 acrosome in around 38% of mature sperm, while their flagellum appeared unaltered and properly
157 connected to the head. *Cylc2*$^{+/-}$ males showed normal sperm tail morphology with around 30% of
158 acrosome malformations. *Cylc2*$^{-/-}$ mature sperm cells displayed morphological alterations of head and
159 mid-piece (Fig. 2 F-G). 76% of *Cylc2*$^{-/-}$ sperm cells showed acrosome malformations, bending of the
160 neck region, and/or coiling of the flagellum, occasionally resulting in its wrapping around the sperm
161 head in 80% of sperm (Fig. 2 F). While 70% of *Cylc1*$^{-/Y}$ *Cylc2*$^{+/-}$ sperm showed these morphological
162 alterations, around 92% of *Cylc1*$^{-/Y}$ *Cylc2*$^{-/-}$ sperm presented with coiled tail and abnormal acrosome
163 (Fig. 2 F-G).

164 To analyze in detail the sperm head, we used Nuclear Morphology software on DAPI stained sperm
165 samples. *Cylc1*$^{-/Y}$ and *Cylc2*$^{+/-}$ sperm showed no alterations of the nuclear shape when compared to
166 wildtype (Fig. 2 H, Fig. S2 C, D). However, heads of *Cylc2*$^{-/-}$ and *Cylc1*$^{-/Y}$ *Cylc2*$^{-/-}$ sperm appeared
167 smaller, with shorter hooks and increased circularity of the nuclei as well as reduced elongation (Fig.
168 2 H, Fig. S2 D). Interestingly, *Cylc1*$^{-/Y}$ *Cylc2*$^{+/-}$ sperm heads appeared unaltered, suggesting that only
169 *Cylc2* has a crucial role for sperm head shaping, and one functional *Cylc2* allele is sufficient to
170 maintain the correct shape of the nucleus (Fig. 2 H, Figure 2 – supplement 3).

171 To study the effects of Cylicin deficiency on sperm calyx integrity and morphology, we analyzed the
172 localization of other calyx-specific proteins, such as CCIN and CapZα3. In epididymal sperm, CCIN co-

173 localize with both CYLC1 and CYLC2 in the calyx (Figure 2 – supplement 4). In *Cylc*1$^{-/y}$ and *Cylc2*$^{+/-}$
174 sperm, CCIN localization remained unchanged, being present in the calyx and in the ventral portion
175 of PT as described previously [7]. However, in 91% of *Cylc2*$^{-/-}$ sperm, CCIN localized to the tail or in
176 random parts of the sperm head (Fig. 2 I, J). In 91% of *Cylc1*$^{-/Y}$ *Cylc2*$^{+/-}$ and 98% of *Cylc1*$^{-/Y}$ *Cylc2*$^{-/-}$
177 sperm, the localization of CCIN was also significantly altered, with the signal mainly being present in
178 the sperm tail. CapZα3 forms a heterodimer with CapZβ3, creating a functional complex that localizes
179 in the calyx [21]. Immunofluorescence stainings revealed that the localization of CapZα3 remained
180 unchanged in *Cylc1*$^{-/Y}$ and *Cylc2*$^{+/-}$ mice compared to wildtype mice. In 84% of *Cylc2*$^{-/-}$ sperm cells,
181 CapZα3 localized in the caudal portion of the head but without regular calyx localization (Fig. 2 I, K).
182 Interestingly, *Cylc1*$^{-/Y}$ *Cylc2*$^{+/-}$ mice showed less severe anomalies of the calyx and although CCIN was
183 located almost exclusively in the tail, CapZα3 maintained the correct calyx localization in around 30%
184 of sperm (Fig. 2 I). Finally, 92% of *Cylc1*$^{-/Y}$ *Cylc2*$^{-/-}$ spermatozoa showed CapZα3 localization across the
185 sperm head without regular calyx shape. These results suggest that the loss of Cylicins impairs the
186 formation of calyx and the correct localization of its components, which might contribute to
187 morphological anomalies of the sperm described initially.

188

189 **_Cylc2_$^{-/-}$ sperm cells have altered flagellar beat**

190 Transmission electron microscopy (TEM) of epididymal sperm confirmed the severe structural
191 defects observed by light microscopy (Fig. 3 A, Figure 3 – supplement 1): *Cylc2*$^{-/-}$ sperm showed
192 coiling of the tail and dislocation of the head-tail connecting piece from the basal plate, resulting in
193 parallel positioning of head and tail (Fig. 3 A, white arrowheads). Furthermore, in *Cylc2*$^{-/-}$ sperm,
194 excess of cytoplasm was observed, located around the nucleus and coiled tail (Fig. 3 A). Anomalies of
195 the head were observed at the level of the PT, while the nuclei appeared unaltered. In all *Cylc2*$^{-/-}$
196 sperm cells, the posterior portion of PT – calyx was absent (Fig. 3 A, red arrowheads). Instead of
197 surrounding the nucleus entirely, the PT in *Cylc2*$^{-/-}$ sperm appeared interrupted, missing completely
198 its caudal part. Further, we observed loosening of the peri-acrosomal region, which is not compact
199 and adherent to the nucleus (Fig. 3 A, green arrowheads). On the contrary, *Cylc1*$^{-/y}$ sperm cells
200 appeared healthy, with intact PT, acrosome and calyx.

201 While the motility of *Cylc1*$^{-/y}$ and *Cylc2*$^{+/-}$ sperm remained unchanged compared to wildtype sperm
202 (around 60% motile cells), motility of *Cylc2*$^{-/-}$ sperm was drastically reduced to only 7% motile sperm
203 (Fig. 3 B) and the motility of *Cylc1*$^{-/y}$ *Cylc2*$^{-/-}$ sperm was reduced to 2% motile sperm. In addition, the
204 few motile sperm cells were not progressive but were swimming in circular trajectories. Interestingly,
205 in *Cylc1*$^{-/y}$ *Cylc2*$^{+/-}$ mice, sperm motility was reduced as well, but less drastically, with 27% of sperm
206 cells being motile (Fig. 3 B).

207 The SpermQ software was used to analyze the flagellar beat of non-capacitated *Cylc2*$^{-/-}$ sperm in
208 detail [22]. *Cylc2*$^{-/-}$ sperm showed stiffness in the neck and a reduced amplitude of the initial flagellar
209 beat, as well as reduced average curvature of the flagellum during a single beat (Figure 3 –
210 supplement 2). Interestingly, we observed that the flagellar beat of *Cylc2*$^{-/-}$ sperm cells was similar to
211 wildtype cells, however, with interruptions during which midpiece and initial principal piece
212 appeared stiff, whereas high frequency beating occurs at the flagellar tip (Fig. 3 C, Video 1, Video 2).
213 These interruptions occurred only on the open-hook side and the duration of such interruptions
214 varied from beat to beat. Of note, similar phenotypes have been observed for sperm with structural
215 defects in the axoneme [23], however axoneme structure of Cylicin-deficient sperm appeared
216 unaltered, presenting typical 9+2 microtubular composition in all genotypes (Figure 3 – supplement
217 1). Thus, we hypothesize that observed structural defects of the PT and head-tail connecting piece
218 are restrictive for sperm motility and physiological beating patterns.

219 Taken together, observed anomalies of sperm heads, impaired sperm motility, and the decrease in
220 epididymal sperm concentration show that Cylicin deficiency resembles a severe OAT (Oligo-
221 Astheno-Teratozoospermia-syndrome) described in human.

222

223 **Cylicins are required for acrosome attachment to the nuclear envelope**

224 To study the origin of observed structural sperm defects, spermiogenesis of Cylicin-deficient males
225 was analyzed in detail. PNA lectin staining and Periodic Acid Schiff (PAS) staining of testicular tissue
226 sections were performed to investigate acrosome biogenesis. During Golgi phase, the acrosome first
227 starts to appear as an aggregation of proacrosomal vesicles into a single granule. This premature
228 acrosomal structure was unaltered in all genotypes, with PNA signal appearing as a small dot on one
229 pole of round spermatids (Fig. 4 A-B). During cap phase, acrosomes grow to cover the apical part of
230 the nucleus. In wildtype and *Cylc2*$^{+/-}$ mice, the forming acrosome appeared equally smooth and
231 showed a regular cap structure on the perinuclear region of round spermatids. However, in some of
232 the round spermatids from *Cylc2*$^{-/-}$ and *Cylc1*$^{-/Y}$ mice, gaps in the forming acrosome were observed, as
233 well as an irregular shape of the cap. In *Cylc1*$^{-/Y}$ *Cylc2*$^{+/-}$ and *Cylc1*$^{-/Y}$ *Cylc2*$^{-/-}$ mice, most of the round
234 spermatids were deformed or displayed irregularly localized caps (Fig. 4 A-B, Figure 4 – supplement
235 1, Figure 4 – supplement 2). At acrosome phase, many elongating spermatids of *Cylc1*$^{-/Y}$, *Cylc2*$^{-/-}$,
236 *Cylc1*$^{-/Y}$ *Cylc2*$^{+/-}$ and *Cylc1*$^{-/Y}$ *Cylc2*$^{-/-}$ mice had irregular acrosome (Fig. 4 A-B, Figure 4 – supplement 1,
237 Figure 4 – supplement 2). Detachment of the acrosome from the nuclear envelope was evident in
238 testis samples of *Cylc2*$^{-/-}$ and *Cylc1*$^{-/Y}$ *Cylc2*$^{-/-}$ male mice. These results suggest that Cylicins are
239 required for the attachment of the developing acrosome to the nuclear envelope during

240 spermiogenesis. Microtubules appeared longer on one side of the nucleus than on the other,
241 displacing the acrosome to the side and creating a gap in the PT (Fig. 4 C). Whereas elongated
242 spermatids at step 14-15 in wildtype sperm already disassembled their manchette and the PT
243 appeared as a unique structure that compactly surrounds nucleus, in *Cylc2*$^{-/-}$ spermatids, remaining
244 microtubules failed to disassemble (Fig. 4 C, yellow arrowhead), and the acrosome detached from
245 the nuclear envelope (green arrowhead). In addition, at step 16, the calyx was absent, and an excess
246 of cytoplasm surrounded the nucleus and flagellum (Fig. 4 C, white arrowhead). Furthermore, many
247 damaged and degrading cells were observed in testicular tissue TEM samples, having perforated
248 nuclei and detached structures (Figure 4 – supplement 3). Interestingly, phagosomes with cellular
249 remains were observed far away from the lumen and sometimes even at the basal membrane of the
250 tubuli, suggesting that the cells that suffer most severe structural damage are being removed. This
251 mechanism of removing malformed cells explains the reduction of epididymal sperm count in Cylicin-
252 deficient genotypes.

253

254 **Cylicin deficiency results in abnormal manchette elongation and disassembly**

255 Next, we investigated the role of Cylicins during formation and development of the manchette – a
256 sperm-specific, transient structure that represents a microtubular platform for protein transport,
257 which showed several anomalies in TEM. Transport of the intracellular vesicles is crucial for the
258 formation of the flagellum, acrosome assembly and removal of excess cytoplasm. The manchette is
259 first detected at step 8 at the perinuclear ring of round spermatids, just prior to their elongation.
260 During the next steps of spermiogenesis, as the spermatids elongate, manchette moves towards the
261 neck region in a skirt-like structure and starts disassembling at step 13 when the elongation is
262 complete [24]. We used immunofluorescence staining of α-tubulin on squash testis samples containing
263 spermatids at different stages of spermiogenesis to investigate whether the altered head shape,
264 calyx structure, and tail-head connection anomalies originate from defects of the manchette
265 structure. Spermatids starting from step 8 were observed individually for step-to-step comparison. In
266 all genotypes, a cap-like shape of the manchette was observed in step 8 round spermatids,
267 suggesting that the manchette assembles properly and starts elongating towards the neck region
268 during step 9 (Figure 5 – supplement 1). In all genotypes, the typical skirt-like structure was observed
269 at the caudal region of the spermatids at step 10 and 11, suggesting that the manchette assembles
270 correctly even in Cylicin-deficient sperm (Fig. 5 A). In spermatids from *Cylc1*$^{-/Y}$ and *Cylc2*$^{+/-}$ mice,
271 regular manchette development was observed in further steps of spermiogenesis (Fig. 5 A). However,
272 starting from step 12, spermatids from *Cylc2*$^{-/-}$, *Cylc1*$^{-/Y}$ *Cylc2*$^{+/-}$, and *Cylc1*$^{-/Y}$ *Cylc2*$^{-/-}$ mice showed
273 abnormal manchette elongation, which became more prominent at step 13 (Fig. 5 A). Manchette

274 length was measured starting from step 10 until step 13 spermatids and the mean was obtained,
275 showing that the average manchette length was 76-80 nm in wildtype, *Cylc1*$^{-/Y}$ and *Cylc2*$^{+/-}$, while for
276 *Cylc2*$^{-/-}$ and *Cylc1*$^{-/Y}$ *Cylc2*$^{-/-}$ spermatids mean manchette length reached 100 nm (Fig. 5 B). *Cylc1*$^{-/Y}$
277 *Cylc2*$^{+/-}$ spermatids displayed an intermediate phenotype with a mean manchette length of 86 nm.
278 Interestingly, some of *Cylc2*-deficient spermatids showed shifting of the manchette to the ventral
279 side of the nucleus along with excessive elongation. At step 16, the manchette was normally
280 disassembled in wildtype, *Cylc1*$^{-/Y}$, and *Cylc2*$^{+/-}$ spermatids (Fig. 5 A). However, *Cylc2* $^{-/-}$, *Cylc1*$^{-/Y}$ *Cylc2*$^{+/-}$
281 , and *Cylc1*$^{-/Y}$ *Cylc2*$^{-/-}$ spermatids showed a persistent α-tubulin signal, indicating that disassembly of
282 the manchette is delayed or incomplete (Fig. 5 A).

283 Other than α-tubulin, we also used HOOK1 as manchette marker. HOOK1 is a member of a family of
284 coiled-coil proteins, which bind to microtubules and organelles and regulate microtubule trafficking
285 during endocytosis and spermiogenesis. Co-staining of the spermatids with antibodies against PNA
286 lectin (green) and HOOK1 (red) revealed that abnormal manchette elongation and acrosome
287 anomalies simultaneously occurred in elongating spermatids of *Cylc2*$^{-/-}$ male mice (Fig. 5 C).
288 Schematic representation shows acrosome biogenesis and manchette development in wildtype and
289 *Cylc2*$^{-/-}$ spermatids (Fig. 5 C). While round spermatids of *Cylc2*$^{-/-}$ mice elongated as those of the
290 wildtype sperm, the manchette elongated abnormally and the acrosome became loosened (Fig. 4 C,
291 Fig. 5 C).

292

293 **_Cylc2_ coding sequence is slightly more conserved among species than _Cylc_1**

294 To address why *Cylc2* deficiency causes more severe phenotypic alterations than *Cylc1* deficiency in
295 mice, we performed evolutionary analysis of both genes. Analysis of the selective constrains on *Cylc1*
296 and *Cylc2* across rodents and primates revealed that both genes' coding sequences are conserved in
297 general, although conservation is weaker in *Cylc1* trending towards a more relaxed constraint (Fig. 6).
298 A model allowing for separate calculation of the evolutionary rate for primates and rodents, did not
299 detect a significant difference between the clades, neither for *Cylc1* nor for *Cylc2*, indicating that the
300 sequences are equally conserved in both clades.

301 To analyze the selective pressure across the coding sequence in more detail, we calculated the
302 evolutionary rates for each codon site across the whole tree. According to the analysis, 34% of codon
303 sites were conserved, 51% under relaxed selective constraint, and 15% positively selected. For *Cylc2*,
304 47% of codon sites were conserved, 44% under neutral/relaxed constraint, and 9% positively
305 selected. Interestingly, codon sites encoding lysine residues, which are proposed to be of functional
306 importance for Cylicins, are mostly conserved. For *Cylc1*, 17% of lysine residues are significantly

307 conserved and 35% of significantly conserved codons encode for lysine. For *Cylc2*, this pattern is even
308 more pronounced with 27.9% of lysine codons being significantly conserved and 24.3% of all
309 conserved sites encoding for lysine (Fig. 6).

310 **Cylicins are required for normal sperm morphology in human**

311 As loss of two Cylicin alleles causes fertility defects in mice, we next addressed whether infertile men
312 also display variants in *CYLC1/CYLC2*.

313 Exome sequencing within the MERGE (**M**al**e** **R**eproductive **G**enomics study) cohort identified one
314 patient (M2270) carrying rare (MAF < 0.01, gnomAD) missense variants in both *CYLC1* and *CYLC2*. The
315 man of German origin presented at age of 40 years for couple infertility because unsuccessfully trying
316 to conceive for 6 years. The couple underwent one ICSI procedure which resulted in 17 fertilized
317 oocytes out of 18 retrieved. Three cryo-single embryo transfers were performed in spontaneous
318 cycles, but no pregnancy was achieved.

319 Patient M2270 carries the hemizygous variant c.1720G>C in *CYLC1* that leads to an amino acid
320 exchange from glutamic acid to glutamine (p.(Glu574Gln)), is predicted to be deleterious or possibly
321 damaging by *in silico* tools (SIFT [25] and PolyPhen [26], respectively), and has a CADD score of 11.91. It is
322 located in exon four out of five and affects a region that is predicted to be intolerant to such
323 substitutions (Figure 7 – supplement 1, metadome). It occurs only twice in the gnomAD database
324 (v2.1.1) comprising 141,456 individuals (67,961 XY), once identified in a hemizygous male and once in
325 a female carrier and is absent from our database.

326 M2270 further carries the heterozygous variant c.551G>A in *CYLC2* that is predicted to be tolerated
327 (SIFT) or benign (PolyPhen) in accordance with a low CADD score of 0.008. It is located in exon five
328 out of eight and affects a region in which variants are likely to be tolerated (Figure 7 – supplement 1,
329 metadome). However, it is a rare variant occurring with an allele frequency of 0.0035 in the general
330 population, according to the gnomAD database. Importantly, only three XX individuals are reported
331 to be homozygous for the variant within *CYLC2*.

332 Segregation analyses revealed maternal inheritance of the X-linked *CYLC1* variant c.1720G>C p.
333 (Glu574Gln), whereas the father carries the heterozygous *CYLC2* variant c.551G>A p.(Gly184Asp) (Fig.
334 7 A). According to ACMG-AMP criteria [27] both variants are classified as variants of uncertain
335 significance. No other potentially pathogenic variants in genes associated with sperm morphological
336 defects were identified by exploring the exome data of M2270.

337 Semen analysis performed following WHO guidelines [28] is shown in Table 1. The sperm concentration
338 in the semen was slightly reduced, while significant reduction of motile spermatozoa (12.5%) was
339 observed. Interestingly, only 2% of the sperm cells appeared morphologically normal, while 98% of

340 sperm showed head defects (Table 1). Immunofluorescence staining of CYLC1 revealed that while in
341 healthy donor's sperm, CYLC1 localizes in the calyx, in M2270, CYLC1 labeling was absent (Fig. 7 B).
342 Bright field microscopy demonstrated that M2270's sperm flagella coiled in a similar manner
343 compared to flagella of sperm from Cylicin-deficient mice. Quantification revealed 57% of M2270
344 sperm displaying abnormal flagella compared to 6% in the healthy donor (Fig. 7 D). Interestingly,
345 DAPI staining revealed that 27% of M2270 flagella carry cytoplasmatic bodies without nuclei and
346 could be defined as headless spermatozoa (Fig. 7 C, white arrowhead; Fig. 7 E). CCIN staining
347 demonstrated that while spermatozoa of a healthy donor showed a typical, funnel-like calyx
348 structure in the posterior region of PT, spermatozoa from M2270 had CCIN localized in irregular
349 manner throughout head and tail, suggesting that Cylicins have a role in maintenance of the calyx
350 structure and composition in both mice and human spermatozoa (Fig. 7 F). Testis-specific
351 phospholipase C zeta 1 (PLCζ1) is localized in the postacrosomal region of PT in mammalian sperm [29]
352 and has a role in generating calcium (Ca^{2+}) oscillations that are necessary for oocyte activation [30].
353 Staining of healthy donor's spermatozoa showed a previously described localization of PLCζ1 in the
354 calyx, while sperm from M2270 patient presents signal irregularly through the PT surrounding sperm
355 heads (Fig. 7 G). These results suggest that Cylicin deficiency can cause severe disruption of PT in
356 human sperm as well, causing male infertility.

357

358 **Discussion**

359 Spermiogenesis is a highly organized process that is dependent on a unique cytoskeletal organization
360 of the sperm cells. The PT has a role of structural scaffold that surrounds sperm nucleus, and its
361 protein composition is crucial for correct sperm development. In this study, we used CRISPR/Cas9
362 gene editing to establish *Cylc1-*, *Cylc2-* and *Cylc1/2*-deficient mouse lines to analyze the role of
363 Cylicins. We demonstrated that the loss of Cylicins impairs male fertility in mice by severely
364 disturbing sperm head architecture. The significance of our findings is supported by the identification
365 of *CYLC1/2* variants in an infertile patient who presents similar structural anomalies in sperm cells.

366 Detailed analysis of sperm development and morphology demonstrated that infertility of Cylicin-
367 deficient male mice is caused by anomalies of different sperm structures. The prominent loss of PT
368 integrity and calyx structure in the mature sperm lead to acrosome loosening and detachment from
369 the nuclear envelope. Furthermore, the shifting of the basal plate caused damage in the head-tail
370 connecting piece resulting in coiling of the flagellum and impaired swimming. Murine Cylicins are first
371 detected in the periacrosomal region of round spermatids and move to the postacrosomal region of
372 PT during spermatid elongation to finally localize to the calyx of mature sperm. This dynamic
373 localization pattern of Cylicins has been described in human, boar and bovine sperm as well [2, 14, 15].

374 Interestingly, other PT enriched proteins CCIN [12, 31, 7] and CPβ3/CPα3 move in the similar manner
375 across PT during spermiogenesis and are present in the calyx of mature sperm of various mammalian
376 species (Figure 2 – supplement 4). This co-localization suggests the potential interaction between
377 calyx proteins. Furthermore, CCIN [2, 12, 13] and CPβ3-CPα3 complex [16–18] are described as actin-binding
378 proteins and porcine Cylc2 has been shown to have a high affinity for F-actin as well [20]. The potential
379 roles of F-actin during spermiogenesis in mammals involve biogenesis of the acrosome [32] and its
380 correct attachment to the outer nuclear membrane of the spermatids [33] as well as removal of excess
381 cytoplasm [34].

382 The loss of Cylicins caused acrosome detachment from NE starting from cap phase of the acrosome
383 biogenesis. Interestingly, loss of CCIN results in similar loosening of the acroplaxome from the outer
384 nuclear membrane [7]. CCIN is shown to be necessary for the IAM-PT-NE complex by establishing
385 bidirectional connections with other PT proteins. Zhang et al. found CYLC1 to be among proteins
386 enriched in PT fraction [7]. Based on their speculation that CCIN is the main organizer of the PT, we
387 hypothesize that both CCIN and Cylicins might interact, either directly or in a complex with other
388 proteins, in order to provide the 'molecular glue' necessary for the acrosome anchoring.
389 Furthermore, Cylicin deficiency resulted in cytoplasmatic retention and bending of the midpiece,
390 similarly to the CPα3 mutant phenotype repro32/repro32 [35]. The CAPZ complex has been shown to
391 regulate the actin dynamics by preventing addition or loss of G-actin subunits to the ends of F-actin
392 filaments [36]. Since we demonstrated that the loss of Cylicins resulted in mislocalization of both CCIN
393 and CPα3, we speculate that Cylicins have a crucial role in maintenance of the integrity of PT
394 structure and thus are required for proper function of PT proteins.

395 Other than morphological defects of the mature sperm PT, during spermiogenesis Cylicin deficiency
396 results in excessive manchette elongation, its delayed disassembly as well as formation of abnormal
397 gaps in the PT at the level of perinuclear ring. The intra-manchette transport (IMT) of proteins from
398 the apical pole of the head to the base of the developing tail occurs during spermiogenesis [37]. The
399 malfunctions of the IMT can cause delay in manchette clearance and morphological defects of
400 mature sperm. Mouse models deficient for IMT proteins such as HOOK1 [38] CEP131 [39] and IFT88 [40]
401 show abnormal manchette elongation and delay in its clearance resulting in aberrant nuclear shape
402 of the sperm. Furthermore, the loss of HOOK1 results in head-tail connection and mid-piece
403 anomalies such as flipping of the head, basal plate defects and coiling of the tail similar to *Cylc2*
404 deficiency [41]. The localization of manchette on the caudal portion of spermatids coincides with the
405 localization of the calyx in the mature sperm, so these results indicate that the manchette might be
406 maintained longer to compensate for the missing formation of the calyx structure. Furthermore, we
407 observed wide gaps in the perinuclear ring during manchette elongation, suggesting that Cylicins

408 might have a role in maintenance of the contact between caudal and apical PT region and its
409 integrity.

410 Our evolutionary analysis of *Cylc1* and *Cylc2* genes across rodents and primates revealed that both
411 coding sequences are under purifying selection. Overall, the results reveal that *Cylc1* is under slightly
412 less conserved constraint than *Cylc2* leading to the hypothesis that loss of function in *Cylc1* might be
413 less severe and could be compensated for by *Cylc2* due to partial redundancy. This hypothesis is
414 supported by our finding that *Cylc1* deficiency causes subfertility in male mice, while the loss of both
415 *Cylc2* alleles results in male infertility. Furthermore, *in Cylc2*$^{+/-}$ male mice fertility was preserved,
416 while *Cylc1*$^{-/Y}$ *Cylc2*$^{+/-}$ males were unable to sire offspring leading to the conclusion that the loss of
417 one *Cylc2* allele could be compensated by *Cylc1*, however at least two functional Cylicin alleles are
418 required for male fertility in mice. Interestingly, *Cylc1*$^{-/Y}$ *Cylc2*$^{+/-}$ males displayed an "intermediate"
419 phenotype, showing slightly less damaged sperm than *Cylc2*$^{-/-}$ and *Cylc1*$^{-/Y}$ *Cylc2*$^{-/-}$ animals. This further
420 supports our notion, that loss of the less conserved *Cylc1* gene might be at least partially
421 compensated by the remaining *Cylc2* allele.

422 In general, the evolutionary rate of C-terminal lysine rich region of both Cylicins seems to be highly
423 volatile between conserved and positively selected codon sites, while the lysine residues seem to be
424 strongly conserved. Changes in the C-terminal region, potentially affecting the length of the lysine
425 rich domain, might have an adaptive advantage. Targeted positive selection on codon sites could also
426 be a signature of co-evolution with a rapidly evolving interactor.

427 Sperm morphological defects and infertility observed in one patient with variants in both Cylicin
428 genes points towards a requirement for human spermiogenesis and fertility. A defect in acrosome
429 formation and the existence of variants in two out of three alleles in both *CYLC* genes is in line with
430 the observations made in mice. The absence of CYLC1 confirmed through immunofluorescent
431 staining indicates a functional impact of the missense variant on the CYLC1 protein. Furthermore,
432 impaired CCIN localization was observed in patient M2270 as well, suggesting that PT has similar
433 roles in human and rodents despite the differences in sperm head shape [42]. These results suggest
434 that establishing mouse models deficient for Cylicin and other PT proteins might provide insights into
435 mechanisms of human spermiogenesis and cytoskeletal regulation as well. However, with our data
436 we cannot exclude the possibility that there is a discrepancy between mice and men and that the
437 missense variant in *CYLC1* might alone be sufficient to cause the observed phenotype of M2270. The
438 o/e ratios of both genes calculated within the gnomAD database rather indicate a stronger selective
439 pressure on human *CYLC1* (0.08) than on *CYLC2* (0.84). Furthermore, the *CYLC1* variant affects an
440 intolerant region within the protein sequence according to metadome [43], whereas the *CYLC2* variant

441 is located in a region that is more tolerant to variation (Figure 7 – supplement 1). Therefore, we
442 cannot definitively validate the hypothesis of an oligogenic disease in men as well.

443 The *CYLC2* missense variant is inherited by the father of M2270 (Fig. 5A) and, thus, not sufficient to
444 cause infertility. However, the father reported difficulties to conceive naturally. Based on this one
445 family, we cannot exclude an effect of pathogenic heterozygous *CYLC2* variants.

446 Overall, the identification and detailed characterization of further patients with variants in *CYLC1* and
447 *CYLC2* is warranted to draw firm conclusions on the effect of variants in these genes on
448 spermiogenesis and infertility.

449

450 **Acknowledgment**

451 This study was supported by a grant from the German Research Foundation (DFG) to HS (SCHO
452 503/23-1, project number 458746826), SS (SCHN 1668/1-1, project number: 458746826) and FT
453 (Clinical Research Unit ‚Male Germ Cells', CRU326). We are grateful to Gaby Beine, Angela Egert,
454 Andrea Jäger, Greta Zech, Luisa Meier and Christina Burhöi for excellent technical assistance. We
455 would like to thank the Core Facilities for Microscopy and Analytical Proteomics of the Medical
456 Faculty at the University of Bonn for providing support and instrumentation funded by the Deutsche
457 Forschungsgemeinschaft (DFG, German Research Foundation, project numbers: 388169927,
458 386936527).

459

460 **Figure legends**

461 **Figure 1: Loss of *Cylc1* or *Cylc2* results in impaired male fertility.**

462 (A) Schematic representation of the *Cylc1* and *Cylc2* gene structure and targeting strategy for CRISPR/Cas9-
463 mediated generation of *Cylc1*- and *Cylc2*-deficient alleles. Targeting sites of guide RNAs are depicted by red
464 arrows. Genotyping primer binding sites are depicted by black arrows.
465 (B) Representative genotyping PCR of *Cylc1*- and *Cylc2*-deficient mice. N=3
466 (C) Fertility analysis of Cylicin-deficient mice visualized by mean litter size and pregnancy rate (%) in
467 comparison to wildtype matings. Black dots represent mean values obtained for each male included in
468 fertility testing. Columns represent mean values +/- standard deviation (SD). Total number of offspring per
469 total number of pregnancies as well as total number of pregnancies per total number of plugs are depicted
470 above each bar.
471 (D) Expression of *Cylc1* and *Cylc2* in testicular tissue of WT, *Cylc1*$^{-/y}$, *Cylc2*$^{+/-}$, *Cylc2*$^{-/-}$, *Cylc1*$^{-/y}$ *Cylc2*$^{+/-}$ and
472 *Cylc1*$^{-/y}$ *Cylc2*$^{-/-}$ mice analyzed by qRT PCR. Biological replicate of 3 was used.

473 (E) Immunofluorescent staining of testicular tissue and cauda epididymal sperm from WT, *Cylc1*$^{-/y}$, *Cylc2*$^{+/-}$,
474 *Cylc2*$^{-/-}$, *Cylc1*$^{-/y}$ *Cylc2*$^{+/-}$ and *Cylc1*$^{-/y}$ *Cylc2*$^{-/-}$ males against CYLC1 and CYLC2. Cell nuclei were counterstained
475 with DAPI. Staining was performed on 3 animals from each genotype. Scale bar: 5 µm.
476 (F) Schematic illustration of CYLC localization during spermiogenesis. CYLC localization (green) is shown for
477 round and elongating spermatids as well as mature sperm.
478 (G) Representative immunoblot against CYLC1 and CYLC2 on cytoskeletal protein fractions from WT, *Cylc1*$^{-/y}$,
479 *Cylc2*$^{+/-}$ and *Cylc2*$^{-/-}$ testes. α-Tubulin was used as load control.

480

481 **Figure 1 – supplement 1:** Amino acid sequence comparison of CYLC1 and CYLC2 in *C.elegans* and *M.musculus*
482 to *H.sapiens*. KKD/E motifs are highlighted in blue and repeating units are marked by red brackets.

483 **Figure 1 – supplement 2:** Immunohistochemical staining against CYLC1 and CYLC2 in tissue sections of testis,
484 brain, thymus and spleen. Scale bar: 100 µm.

485 **Figure 1 – supplement 3:** Immunofluorescence staining against the acrosomal matrix marker protein SP56
486 (green) and CYLC1 or CYLC2 (red) in round and elongating spermatids. Nuclei were stained with DAPI. Scale bar:
487 5 µm.

488 **Figure 1 – supplement 4:** Immunofluorescence staining of CYLC1 and CYLC2 in elongating spermatids of WT,
489 *Cylc1*$^{-/y}$, *Cylc2*$^{+/-}$, *Cylc2*$^{-/-}$, *Cylc1*$^{-/y}$ *Cylc2*$^{+/-}$ and *Cylc1*$^{-/y}$ *Cylc2*$^{-/-}$ mice. Scale bar: 5 µm.

490 **Figure 1 – supplement 5:** Proteome abundances

491 **Figure 1 – supplement 6:** Proteome clustering

492

493 **Figure 2: Sperm morphology is severely altered in Cylicin-deficient mice**

494 (A) Testis weight [mg] and sperm count (x10^{7}) of WT, *Cylc1*$^{-/y}$, *Cylc2*$^{+/-}$, *Cylc2*$^{-/-}$, *Cylc1*$^{-/y}$ *Cylc2*$^{+/-}$ and *Cylc1*$^{-/y}$
495 *Cylc2*$^{-/-}$ males. Mean values +/- SD are shown; block dots represent data points for individual males.
496 (B) Comparable photographs of the testes of WT, *Cylc1*$^{-/y}$, *Cylc2*$^{+/-}$, *Cylc2*$^{-/-}$, *Cylc1*$^{-/y}$ *Cylc2*$^{+/-}$ and *Cylc1*$^{-/y}$ *Cylc2*$^{-/-}$
497 mice.
498 (C) Epididymal sperm count (x10^{7}) of WT, *Cylc1*$^{-/y}$, *Cylc2*$^{+/-}$, *Cylc2*$^{-/-}$, *Cylc1*$^{-/y}$ *Cylc2*$^{+/-}$ and *Cylc1*$^{-/y}$ *Cylc2*$^{-/-}$ males.
499 Mean values +/- SD are shown; block dots represent data points for individual males.
500 (D) Viability of the epididymal sperm stained with Eosin Nigrosine. Percentage of Eosin negative (viable) and
501 Eosin positive (inviable) sperm is shown. Data represented as mean +/- SD. Staining was performed on 3
502 animals from each genotype.
503 (E) Bright field microscopy pictures of epididymal sperm from WT, Cylc1$^{-/y}$, Cylc2$^{+/-}$ and Cylc2$^{-/-}$ mice. Scale bar:
504 10 µm.
505 (F) Immunofluorescence staining of epididymal sperm acrosomes with PNA lectin (green) and tails with
506 MITOred (red). Nuclei were counterstained with DAPI. Scale bar: 5 µm.

507 (G) Quantification of abnormal sperm of WT, *Cylc1*$^{-/y}$, *Cylc2*$^{+/-}$, *Cylc2*$^{-/-}$, *Cylc1*$^{-/y}$ *Cylc2*$^{+/-}$ and *Cylc1*$^{-/y}$ *Cylc2*$^{-/-}$ mice
508 is shown. Acrosome aberrations and tail coiling were counted separately. Staining was performed on 3
509 animals from each genotype.
510 (H) Nuclear morphology analysis of WT, *Cylc1*$^{-/y}$, *Cylc2*$^{+/-}$, *Cylc2*$^{-/-}$, *Cylc1*$^{-/y}$ *Cylc2*$^{+/-}$ and *Cylc1*$^{-/y}$ *Cylc2*$^{-/-}$ sperm.
511 Number of cells analyzed for each genotype is shown.
512 (I) Representative pictures of immunofluorescent staining against PT proteins CCIN (upper panel) and CAPZa3
513 (lower panel) in WT, *Cylc1*$^{-/y}$, *Cylc2*$^{+/-}$, *Cylc2*$^{-/-}$, *Cylc1*$^{-/y}$ *Cylc2*$^{+/-}$ and *Cylc1*$^{-/y}$ *Cylc2*$^{-/-}$ sperm. Nuclei were
514 counterstained with DAPI. Staining was performed on 3 animals from each genotype. Scale bar: 5 µm.

515 (J-K) Quantification of sperm with abnormal calyx integrity in WT, *Cylc1*$^{-/y}$, *Cylc2*$^{+/-}$, *Cylc2*$^{-/-}$, *Cylc1*$^{-/y}$ *Cylc2*$^{+/-}$ and
516 *Cylc1*$^{-/y}$ *Cylc2*$^{-/-}$ mice based on CCIN and CapZA staining patterns.

517 **Figure 2 – supplement 1:** HE-stained testicular tissue sections of WT, *Cylc1*$^{-/y}$, *Cylc2*$^{+/-}$, *Cylc2*$^{-/-}$, *Cylc1*$^{-/y}$ *Cylc2*$^{+/-}$
518 and *Cylc1*$^{-/y}$ *Cylc2*$^{-/-}$ mice. Scale bar: 100 µm.

519 **Figure 2 – supplement 2:** Eosin-Nigrosin staining of epididymal sperm samples from WT, *Cylc1*$^{-/y}$, *Cylc2*$^{+/-}$, *Cylc2*$^{-}$
520 $^{/-}$, *Cylc1*$^{-/y}$ *Cylc2*$^{+/-}$ and *Cylc1*$^{-/y}$ *Cylc2*$^{-/-}$ mice. Scale bar: 10 µm.

521 **Figure 2 – supplement 3:** Nuclei of WT, *Cylc1*$^{-/y}$, *Cylc2*$^{+/-}$, *Cylc2*$^{-/-}$, *Cylc1*$^{-/y}$ *Cylc2*$^{+/-}$ and *Cylc1*$^{-/y}$ *Cylc2*$^{-/-}$ sperm
522 stained with DAPI. Scale bar: 5 µm. Elongation and circularity of nuclei from WT, *Cylc1*$^{-/y}$, *Cylc2*$^{+/-}$, *Cylc2*$^{-/-}$, *Cylc1*$^{-}$
523 $^{/y}$ *Cylc2*$^{+/-}$ and *Cylc1*$^{-/y}$ *Cylc2*$^{-/-}$ sperm. The minimum detection area was set to 1.000 pixels, while the maximum
524 detection area was 7.000 pixels.

525 **Figure 2 – supplement 4:** Co-staining against CYLC1/CYLC2 (red) and CCIN (green) in epididymal sperm cells of
526 WT mouse. Nuclei were counterstained with DAPI. Scale bar: 2 µm.

527

528 **Figure 3: *Cylc2*$^{-/-}$ sperm cells have altered flagellar beat**

529 (A) TEM micrographs of WT, *Cylc1*$^{-/y}$ and *Cylc2*$^{-/-}$ epididymal sperm. Acrosome appears detached from the
530 nucleus in *Cylc2*$^{-/-}$ sperm (green arrowheads), while the calyx is missing entirely (red arrowheads). The
531 head-tail connecting piece shifted from the basal plate is shown by white arrowheads causing the looping
532 of the flagellum and formation of a cytoplasmatic sac. *Cylc1*$^{-/y}$ sperm appears comparable to WT. Scale bar:
533 1 µm.
534 (B) Motility of the epididymal sperm of WT, *Cylc1*$^{-/y}$, *Cylc2*$^{+/-}$, *Cylc2*$^{-/-}$, *Cylc1*$^{-/y}$ *Cylc2*$^{+/-}$ and *Cylc1*$^{-/y}$ *Cylc2*$^{-/-}$ males
535 activated in TYH medium.
536 (C) Full and half-beat cycle plots of the flagellar beat are shown for WT and *Cylc2*$^{-/-}$ spermatozoa. Half beat
537 cycle shows the stiffness of the midpiece (upper arrow) and high oscillations (lower arrow) in *Cylc2*$^{-/-}$ sperm
538 in one direction of the beat.

539 **Figure 3 – supplement 1:** TEM micrographs of WT and *Cylc2*$^{-/-}$ sperm and axonemes.

540 **Figure 3 – supplement 2:** SpermQ analysis of the flagellar beat of WT (green) and *Cylc2*$^{-/-}$ (red) sperm. Average
541 curvature of the flagellum and the arc length are shown.

542

543 **Figure 4: Cylicins are required for acrosome attachment to the nuclear envelope**

544 (A) PNA-FITC lectin immunofluorescence staining of the acrosome in testicular tissue of WT, *Cylc1*$^{-/y}$, *Cylc2*$^{+/-}$,
545 *Cylc2*$^{-/-}$, *Cylc1*$^{-/y}$ *Cylc2*$^{+/-}$ and *Cylc1*$^{-/y}$ *Cylc2*$^{-/-}$ mice (green). Golgi phase of acrosome biogenesis at round
546 spermatid stage (I-IV) is visible in the left panel. Middle panel shows cap phases on round spermatids
547 (stage V-VIII). In the right panel acrosomal phase is shown (stage IX-XI). Nuclei were counterstained with
548 DAPI. Staining was performed on 3 animals from each genotype. Scale bar: 10 µm. Insets show
549 representative single spermatids at higher magnification (scale bar: 2 µm).
550 (B) PAS staining of testicular sections from WT, *Cylc1*$^{-/y}$, *Cylc2*$^{+/-}$, *Cylc2*$^{-/-}$, *Cylc1*$^{-/y}$ *Cylc2*$^{+/-}$ and *Cylc1*$^{-/y}$ *Cylc2*$^{-/-}$
551 mice. Representative spermatids at different steps of spermiogenesis are shown. Scale bar: 3 µm.
552 (C) TEM micrographs of testicular tissues of WT and *Cylc2*$^{-/-}$ mice. Single spermatids from step 6 to step 16 are
553 shown. nu: nucleus; av: acrosomal vesicle; pr: perinuclear ring; m: manchette microtubules; cy: cytoplasm;
554 green arrowheads: developing acrosome; red arrowheads: manchette; white arrowhead: cytoplasm;
555 yellow arrowhead: remaining microtubules in mature sperm. Scale bar: 1 µm.
556

557 **Figure 4 – supplement 1:** PNA-lectin immunofluorescence staining of WT, *Cylc1*$^{-/y}$, *Cylc2*$^{+/-}$, *Cylc2*$^{-/-}$, *Cylc1*$^{-/y}$
558 *Cylc2*$^{+/-}$ and *Cylc1*$^{-/y}$ *Cylc2*$^{-/-}$ testicular tissue. Spermatids at cap phase and acrosome phase of acrosome
559 biogenesis are shown individually. Scale bar: 5 µm.

560 **Figure 4 – supplement 2:** PAS stained testicular tissue sections of WT, *Cylc1*$^{-/y}$, *Cylc2*$^{+/-}$, *Cylc2*$^{-/-}$, *Cylc1*$^{-/y}$ *Cylc2*$^{+/-}$
561 and *Cylc1*$^{-/y}$ *Cylc2*$^{-/-}$ mice. Scale bar: 20 µm.

562 **Figure 4 – supplement 3:** TEM micrographs of degrading damaged spermatids in testicular sections of *Cylc2*$^{-/-}$
563 mice. Scale bar: 5 µm.

564

565 **Figure 5: Cylc2 deficiency causes delay in manchette removal**

566 (A) Immunofluorescence staining of α-Tubulin to visualize manchette structure in squash testis samples of WT,
567 *Cylc1*$^{-/y}$, *Cylc2*$^{+/-}$, *Cylc2*$^{-/-}$, *Cylc1*$^{-/y}$ *Cylc2*$^{+/-}$ and *Cylc1*$^{-/y}$ *Cylc2*$^{-/-}$ mice. Spermatids in different steps of
568 spermiogenesis were shown, for step-to-step comparison. Scale bar: 5 µm.
569 (B) Quantification of manchette length in WT, *Cylc1*$^{-/y}$, *Cylc2*$^{+/-}$, *Cylc2*$^{-/-}$, *Cylc1*$^{-/y}$ *Cylc2*$^{+/-}$ and *Cylc1*$^{-/y}$ *Cylc2*$^{-/-}$ α-
570 Tubulin stained spermatids at step 10-13.
571 (C) Co-staining of the manchette with HOOK1 (red) and acrosome with PNA-lectin (green) is shown in round,
572 elongating and elongated spermatids of WT (upper panel) and *Cylc2*$^{-/-}$ mice (lower panel). Scale bar: 3 µm.
573 Schematic representation shows acrosomal structure (green) and manchette filaments (red).

574

575 **Figure 5 – supplement 1:** Immunofluorescence staining of α-Tubulin in WT, *Cylc1*$^{-/y}$, *Cylc2*$^{+/-}$, *Cylc2*$^{-/-}$, *Cylc1*$^{-/y}$
576 *Cylc2*$^{+/-}$ and *Cylc1*$^{-/y}$ *Cylc2*$^{-/-}$ squash testis samples. Spermatids at step 8-9 are shown. Scale bar: 10 µm.

577

578 **Figure 6:** Species phylogeny with branch length representing number of nucleotide substitutions per codon
579 with
580 schematic representation of (A) CYLC1 and (B) CYLC2 amino acid alignment used in the PAML CodeML analysis.
581 Alignments were stripped of columns with gaps in more than 80% of species. Evolutionary rate (ω) obtained by
582 CodeML models M0 is shown for the whole alignment. The graph on top shows the evolutionary rate (ω) per
583 codon sites across the whole tree (CodeML model M2a). Significantly positively selected sites are marked by
584 asterisks. Sites with a probability of higher than 0.95 to belonging to the conserved or positively selected site
585 class are marked in green and red respectively below the graph.

586

587 **Figure 7: Cylicins are required for human male fertility**

588 (A) Pedigree of patient M2270. His father (M2270_F) is carrier of the heterozygous *CYLC2* variant c.551G>A
589 and his mother (M2270_M) carries the X-linked *CYLC1* variant c.1720G>C in a heterozygous state. Asterisks
590 (*) indicate the location of the variants in *CYLC1* and *CYLC2* within the electropherograms.
591 (B) Immunofluorescence staining of CYLC1 in spermatozoa from healthy donor and patient M2270. In donor's
592 sperm cells CYLC1 localizes in the calyx, while patient's sperm cells are completely missing the signal. Scale
593 bar: 5 µm.
594 (C) Bright field images of the spermatozoa from healthy donor and M2270 show visible head and tail
595 anomalies, coiling of the flagellum as well as headless spermatozoa, which carry cytoplasmatic residues
596 without nuclei (white arrowhead). Heads were counterstained with DAPI. Scale bar: 5 µm.

597 (D-E) Quantification of flagellum integrity (D) and headless sperm (E) in the semen of patient M2270 and a
598 healthy donor.

599 (F-G) Immunofluorescence staining of CCIN (F) and PLCz (G) in sperm cells of patient M2270 and a healthy
600 donor. Nuclei were counterstained with DAPI. Scale bar: 3 µm.

601

602 **Figure 7 – supplement 1:**

603 (A) Localization of the CYLC1 variant found in M2270. The variant affects exon four and an intolerant part of
604 the C-terminal region of CYLC1 according to metadome 41.
605 (B) CYLC2 variant localization. The missense variant in CYLC2 detected in M2270 affects exon five and a
606 tolerant part of CYLC2 according to metadome 41.

607

608 **Table 1:** Semen analysis of the patient M2770 carrying variants in the *CYLC1* and *CYLC2* genes

	First visit	Second visit	WHO reference rang
Abstinence time [d]	4.0	5.0	
Volume [ml]	4.2	5.8	> 1.4
Concentration [Mill./ml]	10.5	16.3	> 16
Total sperm count [Mill.]	44.1	94.5	> 39
Vitality [%]	53	27	> 54
Motility			
a [%]	7	9	a + b >30
b [%]	5	4	
c [%]	19	8	
d [%]	69	79	
Morphology			
Normal [%]	2	2	> 4
Head defects [%]	99	99	
Midpiece defects [%]	63	59	
Flagella defects [%]	18	47	

609

610 **Table 2: Protospacer sequences**

Name	protospacer sequence (5´-3´)
Mm.Cas9.CYLC1.sg1	GGTTTATCCATACGTGAGT
Mm.Cas9.CYLC1.sg2	GGCTTAGGTGATGCTCTAAA
Mm.Cas9.CYLC2.1.AB	AAGGGAGAGTCGAAAAGCGT
Mm.Cas9.CYLC2.1.AF	GGATCCAAGGATAAAGTGTC

611

612 **Table 3: PCR primer sequences**

Cylc1	5´-3´	expected band size
Cylc1_F1	TATACACACAATCCACAATCTTGAAAT	WT: 427 bp
Cylc1_R1	TCACTTCAAAATCCAACTTGTCCT	*KO: 264 bp*
Cylc1_R2	TGCCTAGTATTTCAGGTTCCCC	
Cylc2		
Cylc2_F1	ACCACCATTATGGATGCACCG	WT: 376 bp
Cylc2_R1	AGTGTTTCTTGTGAGCTCGTTG	KO: 286 bp

Cylc2_R2	GGCTGAATCTTTACCCTTAGGT	

613

614 **Table 4: qRT primer sequences**

Name	forward (5´-3´)	reverse (5´-3´)
Cylc1	GGGGAAAAATAAGCTCATGTGTAG	TTCAGGTTCCCCATTGGTTA
Cylc2	GCATTTCCCAAACCACCAAGG	AACGGATGGTCTCTCGGATATT
beta-actin	TGTTACCAACTGGGACGACA	GGGTGTTGAAGGTCTCAAA

615

616 **Table 5: Antibodies**

Antibody	**company**	**Catalogue number**	**Antigen**	**Dilution IF**	**Dilution WB**
α-Tubulin	Abcam	ab7291			1:10000 in 3% BSA
α-Tubulin	Merck Millipore (Billerica, USA)	16-232		1:1000	
CapZa3	Progen	GP-SH4		1:500	
Ccin	Progen	GP-SH3		1:500	
Cylc1 (used for mouse)	Davids Biotechnology (Regensburg, Germany)	Custom made polyclonal antibody	AESRKSKNDERRKTLKIKFRGK and KDAKKEGKKKGKRESRKKR	1:1000 (sperm cells) 1:500 (testis tissue) 1:1000 Western blot	1:1000 in 5% milk in TBST
Cylc1 (used for human samples)	Santa Cruz	sc-166400		1:500	
Cylc2	Davids Biotechnology (Regensburg, Germany)	Custom made polyclonal antibody	KSVGTHKSLASEKTKKEVK and ESGGEKAGSKKEAKDDKKDA	1:1000 (sperm cells) 1:500 (testis tissue) 1:1000 Western blot	1:1000 in 5% milk in TBST
Hook1	Proteintech	10871-1-AP		1:500	

PLCζ	Invitrogen	PA5-50476		1:100	
Sp56	Invitrogen	MA1-10866		1:500	

617

618 **Methods**

619 **Animals**

620 All animal experiments were conducted according to German law of animal protection and in
621 agreement with the approval of the local institutional animal care committees (Landesamt für Natur,
622 Umwelt und Verbraucherschutz, North Rhine-Westphalia, approval IDs: AZ84-02.04.2013.A429,
623 AZ81-02.04.2018.A369). *Cylc1*- and *Cylc2*-deficient mice were generated by CRISPR/Cas9-mediated
624 gene-editing in zygotes of the hybrid strain B6D2F1. Guide sequences are depicted in Table 2. For
625 *Cylc1*, in vitro transcribed sgRNAs (50 ng/µl each) and Cas9 mRNA (100 ng/µl) (Sigma-Aldrich,
626 Taufkirchen, Germany) were microinjected into the cytoplasm of zygotes as described previously [44].
627 *Cylc2*-deficient mice were generated by electroporation of ribonucleoprotein (RNP) complexes into
628 zygotes using a GenePulser II electroporation device (BioRad, Feldkirchen, Germany). For RNP
629 formation, crRNA and tracrRNA (IDT, Leuven, Belgium) were combined in duplex buffer (IDT) to a
630 final concentration of 50 mM each and annealed (95°C, 5 min; cool down to room temperature with -
631 0,2°C/sec.). For RNP assembly, 4 µM Cas9 protein (IDT) and 2 µM of each annealed cr/tracr RNA were
632 combined in Opti-MEM media (Gibco 11058-021, Thermo Fisher, Carlsbad, USA) and incubated for 10
633 min at room temperature. RNPs complexes were diluted 1:2 in Opti-MEM, supplemented with 30-40
634 zygotes in a 0.1 cm gene-pulser cuvette (BioRad) and electroporated (two 30 V square wave pulses, 2
635 ms pulse length, 100 ms pulse interval). Recovered embryos were cultured over night at 37°C, 5%
636 CO_2 in G-TL medium (Vitrolife, Göteborg, Sweden) and transferred into the oviduct of
637 pseudopregnant CB6F1 foster mice at 2-cell stage. Offspring were genotyped and gene-edited alleles
638 were separated by backcrossing of founder animals with C57Bl/6J mice. Established mouse lines
639 were registered with Mouse Genome Informatics: Cylc1^{em1Hsc} (MGI: 7341368), Cylc2^{em1Hsc}
640 (MGI:6718280). Mouse lines were maintained as congenic strains on C57Bl/6J background. For all
641 analyses sexually mature males at the age of 8-15 weeks, backcross generation ≥N3 were used.

642 **Genomic DNA extraction and genotyping**

643 Genomic DNA was extracted from biopsies using the HotShot method [45]. PCR reactions were
644 assembled according to the manufacturers protocol of the DreamTaq Green DNA Polymerase
645 (Thermo Fisher, EP0712) using gene-specific primers listed in Table 3.

646 **Fertility analysis**

647 Males were mated 1:2/1:1 with C57Bl/6J females, which were checked daily for presence of a vaginal
648 plug indicative for successful copulation. Plug positive females were separated and pregnancies as
649 well as litter size were recorded.

650 **Sampling**

651 Mature sperm were obtained from the cauda epididymis in M2 medium (Merck) or PBS preheated at
652 37°C. Following several incisions of the cauda, sperm were retrieved by flush-out for 15-30 min. The
653 extracted sperm samples were washed in PBS, centrifuged (4000 rpm, 5 min, 4°C) and snap frozen.
654 For squash tubule samples, fresh testes from three animals of each genotype were transferred to PBS
655 and tubules were dissected as described by Kotaja et al. [46]. Tubule sections were pressed on a slide,
656 quickly frozen in liquid nitrogen and fixed in 90% ethanol for 5 min.

657 **Semen analysis**

658 Sperm concentrations for at least 4 animals of each genotype were determined using a Neubauer
659 hemocytometer. Viability of sperm was determined by Eosin-Nigrosin staining as described
660 previously [47] for at least 3 animals per genotype. Sperm motility was analyzed referring to the WHO
661 guidelines for analysis of human semen. For all analyses at least 100 sperm per individual were
662 analyzed and the percentage of motile/immotile, viable/inviable sperm was calculated.

663 **Quantitative reverse transcription-polymerase chain reaction (qRT-PCR)**

664 RNA was extracted from the testis tissue with TRIzol (Life Technologies, Carlsbad, USA; 15596018).
665 RNA concentrations and purity ratios were determined by NanoDrop ONE (Thermo Scientific)
666 measurements. qRT-PCR was performed as described previously [42], on ViiA 7 Real Time PCR System
667 (Applied Biosystems) using Maxima SYBR Green qPCR Mastermix (Thermo Fisher; K0221). Replicate
668 of 3 was used for each genotype. Beta-actin was used as a housekeeping gene for normalization.
669 Primers used are shown in table 4.

670 **Subcellular protein extraction and Western Blot analysis**

671 For the extraction of cytoskeletal protein fraction from sperm cells, Subcellular Fractionation Kit for
672 Cultured cells (Thermo Fisher, #78840) was used according to manufacturer's instructions, with slight
673 modifications to adjust it to sperm cells. Five subcellular protein fractions were extracted: membrane
674 protein fraction, cytoplasmic protein fraction, soluble nuclear fraction, chromatin bound fraction and
675 cytoskeletal protein fraction. Briefly, epididymal sperm cells were washed in ice cold PBS and
676 centrifuged at 500 x g for 5 min at 4°C. Pellet was resuspended in Cytoplasmatic Extraction Buffer
677 (CEB), incubated for 10 min and centrifuged again at 500 x g for 5 min. Following steps of subcellular
678 fractionation were performed according to manufacturer's instructions. Quantity of proteins in each

679 fraction was determined using NanoDrop ONE (Thermo Fisher). For further analysis only cytoskeletal
680 protein fraction was used.

681 Cytoskeletal proteins were separated on 12% SDS gel with 5% stacking gel. Transfer to PVDF
682 membrane was performed using Trans Blot Turbo System (Bio-Rad). Membranes were washed with
683 TBST 1X, stained with Coomassie blue and blocked with 1% milk for 1 h at room temperature with
684 gentle shaking. Primary antibodies anti-CYLC1 and anti-CYLC2 were diluted in milk and incubated
685 overnight at 4°C (for antibody dilutions see table 5). After washing in TBST, membranes were
686 incubated for 1 h at room temperature with polyclonal goat anti-rabbit secondary antibody IgG/HRP
687 (P044801-2; Agilent Technologies/Dako, Santa Clara, 527 CA, United States) diluted 1:2000 in milk.
688 After extensive TBST washing membranes were imaged using WESTARNOVA2.0 chemiluminescent
689 substrate (Cyanagen) or SuperSignal West Femto Maximum Sensitivity Substrate (34095; Thermo
690 Fisher) and ChemiDoc MP Imaging system (Bio-Rad). Membranes were further re-blocked in 3% BSA
691 for 1 h at room temperature with gentle shaking and incubated with α-Tubulin at 4°C overnight. After
692 washing in TBST, membranes were incubated for 1 h at room temperature with polyclonal rabbit
693 anti-mouse secondary antibody IgG/HRP (P0260; Agilent Technologies/Dako) diluted 1:2000 in 3%
694 BSA.

695 **Proteomics**

696 Peptide preparation

697 All chemicals from Sigma unless otherwise noted.

698 Cytoskeletal protein solutions extracted as described in previous paragraph were processed with the
699 SP3-approach [48]. Briefly, protein lysate with 50 µg protein were subjected to cysteine reduction and
700 alkylation with 20 mM DTT and 40 mM acrylamide in 50 mM triethylammonium bicarbonate (TEAB).
701 Then a mixture of hydrophilic carboxylate-coated magnetic beads (equal amounts of Sera-Mag
702 SpeedBeads, GE Healthcare, cat. no. 45152105050250, and cat. no. 65152105050250) were added at
703 a bead:protein ratio of 10:1 (w/w). Protein binding was induced by adding 3 volumes of ethanol and
704 subsequent mixing for 5 min. Beads with bound proteins were then washed three times with 80%
705 ethanol and finally subjected to overnight tryptic digestion at 37 °C using a trypsin:protein ratio of
706 1:25. Peptide solutions were separated from the magnetic beads, dried in a vacuum concentrator,
707 and stored at -20°C. Before measurements, 10 µg of peptides were further desalted with C18 ZipTips
708 (Merck Millipore, Darmstadt, Germany) to ensure complete removal of beads.

709 LC-MS analysis

710 Dried peptides were dissolved in 10 µl 0.1% formic acid (solvent A) Peptide separation was
711 performed on a Dionex Ultimate nano HPLC system (Dionex GmbH, Idstein, Germany) coupled to an
712 Orbitrap Fusion Lumos mass spectrometer (Thermo Fisher Scientific, Bremen, Germany). 1 µg
713 peptides were injected onto a C18 analytical column (400 mm length, 100 µm inner diameter,
714 ReproSil-Pur 120 C18-AQ, 3 µm).

715 The samples were analyzed by a standard data-dependent (DDA) method: Peptides were separated
716 during a linear gradient from 5% to 35% solvent B (90% acetonitrile, 0.1% FA) at 300 nL/min within
717 120 min. Data-dependent acquisition was performed on ions between 330 and 1600 m/z scanned in
718 the Orbitrap detector every 2.5 seconds (R=120,000, standard gain control and inject time settings).
719 Polysiloxane (*m/z* 445.12002) was used for internal calibration. z>1 ions were subjected to higher-
720 energy collision induced dissociation (HCD: 1.0 Da quadrupole isolation, threshold intensity 25,000,
721 collision energy 28%) and fragments analyzed in the Orbitrap (R=15,000). Fragmented precursor ions
722 were excluded from repeated analysis for 25 s.

723 Data analysis

724 Raw data processing of DDA data and analysis of database searches were performed with Proteome
725 Discoverer software 2.5.0.400 (Thermo Fisher Scientific). Peptide identification was done with an in-
726 house Mascot server version 2.8.1 (Matrix Science Ltd, London, UK) against the Uniprot reference
727 proteome for Mus musculus (as of 06/28/23) and a collection of common contaminants [49]. Precursor
728 ion *m/z* tolerance was 10 ppm, fragment ion tolerance 20 ppm. Tryptic peptides (Trypsin/P) with up
729 to two missed cleavages were searched, propionamide was set as a static modification of cysteines,
730 while oxidation of methionine and acetylation of protein N-termini were set as dynamic
731 modifications. Spectrum confidence of Mascot results was assessed by the Percolator algorithm 3.05
732 as implemented in Proteome Discoverer [50]. Spectra without high confident matches (q-value > 0.01)
733 were sent to a second round Mascot search with semi-specific enzyme cleavage and changing the
734 modification of cysteines with propionamide to dynamic. Proteins with two unique proteins in the
735 protein group were reported. For quantification, summed abundances were normalized on total
736 protein amount in Proteome Discoverer.

737

738 **High-resolution microscopy of the flagellar beat**

739 Image sequences of mouse sperm were acquired using dark-field at an inverted microscope (IX71;
740 Olympus, Hamburg, Germany), equipped with a dark-field condenser and a high-speed camera
741 (ORCA-Flash4.0 V3, C13220-20 CU, Hamamatsu, Hamamatsu City, Japan). A 10x objective (NA 0.4,
742 UPlanFL; Olympus, Hamburg, Germany) with an additional 1.6x magnifying lens (Olympus, Hamburg,

743 Germany) that was inserted into the light path (final magnification: 16x) was applied. Image
744 sequences were recorded at a rate of 200 frames per second (fps). A custom-made observation
745 chamber was used [22]. Sperm samples were diluted in THY buffer shortly before insertion of the
746 suspension into the observation chamber. Three WT and three *Cylc2*$^{-/-}$ animals were used.

747 **Sperm nuclear morphology**

748 For the analysis of sperm nuclear morphology, epididymal sperm samples from 3 animals of each
749 genotype were fixed in methanol and acetic acid (3:1). The samples were spread onto a slide and
750 stained with 4‘,6-diamidino-2-phenylindole (DAPI) containing mounting medium (ROTImount
751 FluorCare DAPI (Carl Roth GmbH, Karlsruhe, Germany; HP20.1)). The sperm cells were imaged at
752 100x magnification, using a Leica DM5500 B fluorescent microscope. At least 200 pictures were taken
753 from each group and analyzed using Nuclear Morphology software [51] according to the developer’s
754 instructions. The minimum detection area was set to 1.000 pixels while the maximum detection area
755 was 7.000 pixels.

756 **Histology**

757 Bouin fixed testis tissues were paraffinized, embedded and sectioned at 3-5 µm using microtome. For
758 histological analysis, the sections were deparaffinized, hydrated incubated with Periodic acid (0.5%)
759 for 10 min, rinsed with H_20 and incubated for 20 min with Schiff reagent. Alternatively, tissue
760 sections were stained with Hemalum solution acid (Henricks and Mayer) and Eosin Y solution (Carl
761 Roth). In both procedures, stained sections were dehydrated in alcohol row and mounted using
762 Entellan (Sigma-Aldrich). Slides were imaged at 20x and 63x magnification under bright field using
763 5500 B microscope.

764 **Immunofluorescence/Immunohistochemistry**

765 Bouin fixed testis tissue sections were deparaffinized in Xylene and rehydrated in decreasing alcohol
766 to be used for immunohistochemical staining. Squash testis samples fixed in 90% EtOH were used for
767 the staining of α-Tubulin and HOOK1. For sperm immunofluorescence, mature sperm cells isolated
768 from cauda epididymis were fixed with methanol acetic acid (3:1), dropped on glass slides and air
769 dried. After washing in PBS twice, all samples were permeabilized using 0.1% Triton x100 for 10 min
770 at room temperature. The samples were then blocked with 5% BSA for 30 min, followed blocking
771 with normal horse serum (Vectorlabs, Burlingame, USA; DI-1788) for 30 min at room temperature.
772 For tissue sections, heat-activated antigen retrieval was performed using citrate buffer (pH 6.0). All
773 primary antibodies were incubated over night at 4°C. Antibodies and dilutions are listed in table 5.
774 The respective secondary antibodies were incubated for 1 h at room temperature using VectaFluor
775 Labeling Kit DyLight 488 and DyLight 594 (Vectorlabs, Burlingame, USA; DI-1788, DI-1794). Slides

776 were mounted with DAPI containing mounting medium (ROTImount FluorCare DAPI, Carl Roth;
777 HP20.1).

778 For IHC staining against CYLC1 and CYLC2, after antigen retrieval and blocking procedures, slides
779 were treated with 6% H_20_2 for 30 min. Slides were then incubated with primary antibodies overnight
780 at 4°C. Biotinylated goat anti-rabbit IgG was used as a secondary antibody and incubated for 1 h at
781 room temperature. Slides were then processed using Vectastain ABC-AP Kit (Vector Laboratories, AK-
782 5001) and stained using ImmPACT® Vector® Red Substrate Kit, Alkaline Phosphatase (Vector
783 Laboratories, SK-5105) according to manufacturer's instructions. Counterstaining was performed
784 using Hematoxylin.

785 For the analysis of acrosome biogenesis peanut agglutinin (PNA)-fluorescein isothiocyanite (FITC)
786 Alexa Fluor 488 conjugate (Molecular Probes, Invitrogen, Waltham, USA; L21409) was used on the
787 Buin fixed testis tissues. After permeabilization and blocking, the tissues were incubated with PNA-
788 FITC 5 µg/ml for 30 min at room temperature. Mature sperm were fixed with paraformaldehyde (4%)
789 for 20 min at room temperature. After PBS washing, the sperm samples were incubated with 5 µg/ml
790 PNA-FITC and 5 nM Mito Tracker Red (Cell Signaling; 9082) for 30 min at room temperature. The
791 slides were then mounted with DAPI mount. All stainings were performed on minimum of 3 animals
792 per genotype.

793 **Transmission electron microscopy**

794 For Transmission Electron Microscopy fresh epididymal sperm and testis tissue were used. After
795 washing with PBS, the samples were fixed in 3% glutaraldehyde at 4°C overnight. The samples were
796 then washed in 0.1 M cacodylate buffer and fixed again in 2% osmium tetroxide at 4% for 2 h. After
797 dehydration in an ascending ethanol row, the samples were contrasted in 70% ethanol 0.5% uranyl
798 acetate for 1.5 h at 4°C. Samples were then washed in propylenoxide, three times for 10 min at room
799 temperature before embedding in Epon C at 70°C for 48 h. Ultra-thin sections were examined using
800 a Verios 460L microscope (FEI) with a STEM III-detector.

801 **Evolutionary analysis**

802 Evolutionary rates of mammalian Cylicin genes were analyzed according to Lüke et al (2016) [52].
803 Briefly, *Cylc1* and *Cylc2* nucleotide sequences were obtained from NCBI genbank and Ensembl
804 genome browser. Phylogenetic trees of considered species were built according to the "Tree of Life
805 web project". The webPRANK software was applied for codon-based alignment of orthologous gene
806 sequences and results were visualized using the ETE toolkit. To determine evolutionary rates of gene
807 sequences across mammals, for different clades and for individual codon sites, the codeml
808 application implemented in the PAML software was used [53, 54]. Selective pressures on protein level

809 are represented by calculation of the nonsynonymous/synonymous substitution rate ratio (ω =
810 dN/dS). It distinguishes between purifying selection (ω<1), neutral evolution (ω=1) and positive
811 selection (ω>1) within various models. The M0 model served as basis for all performed analyses.
812 Different codon frequency settings were tested for the M0 model of each gene and the setting with
813 the highest likelihood was chosen. To test whether alternative models describe the selective
814 constraints within a dataset more precise than the M0 model, likelihood ratio-tests (LRT) were
815 performed. Applied models and LRTs are described by Yang [53, 54] and Lüke et al. [52].

816 **Study cohort and ethical approval**

817 The MERGE (**M**al**e** **R**eproductive **G**enomics study) cohort currently comprises over 2,030 men, mainly
818 recruited at the Centre of Reproductive Medicine and Andrology (CeRA) in Münster. The large
819 majority has severe spermatogenic failure, i.e. severe oligozoospermia (<5 Mill./ml sperm
820 concentration), crypto- or azoospermia. So far, only 35 cases were included because of notable
821 sperm morphological defects (≥5 Mill./ml sperm concentration, <4 % normal forms). Common causes
822 for infertility such as oncologic diseases, AZF deletions or chromosomal aberrations were ruled out in
823 advance. Patients with aetiologically still unexplained infertility underwent whole exome sequencing.

824 All participants gave written informed consent according to the protocols approved by the Ethics
825 Committee of the Medical Faculty Münster (Ref. No. MERGE: 2010-578-f-S) in accordance with the
826 Declaration of Helsinki in 1975.

827 **Whole exome sequencing and data analysis**

828 After DNA extraction from patients' peripheral blood lymphocytes WES was performed as previously
829 described [55]. WES data obtained from 2,066 infertile men was filtered for rare (≤ 0.01 minor allele
830 frequency, gnomAD) variants located within the coding sequence or the adjacent 15 bp of flanking
831 introns in *CYLC1* and *CYLC2*. Patients carrying only one variant in either of the gene were excluded. In
832 case of either bi-allelic *CYLC2* variants or a combination of *CYLC1* and *CYLC2* variants, the whole
833 exome dataset was screened to rule out other potential genetic causes. Variants detected in this
834 study were classified according to the guidelines by the American College of Medical Genetics and
835 Genomics-Association for Molecular Pathology (ACMG-AMP) [27] adapted to recent recommendations
836 as outlined in [56].

837 To rule out an alternative genetic cause for the patient's condition, his exome data was screened for
838 rare (MAF ≤ 0.01, gnomAD and in-house database), homozygous, X-linked or potentially compound
839 heterozygous high-impact variants (stop gain, start lost, stop lost, frameshift, splice site and splice
840 region as well as missense variants with CADD > 20) and rare, heterozygous LoF variants (stop gain,

841 start lost, stop lost, frameshift, splice site) without filtering for a specific set of genes. Respective
842 genes were screened for testis-expression and reports of infertility.

843 **Sanger sequencing**

844 Sanger sequencing with variant-specific primers was conducted for validation and segregation
845 purposes. The primers to confirm the *CYLC1* (NM_021118.3) variant c.1720G>C p.(Glu574Gln) are
846 5'-ACTGATGCTGACTCTGAACCG-3' (forward) and 5'-CCTTCGAGTCACAAAGTTGTCA-3' (reverse). To
847 confirm the *CYLC2* (NM_001340.5) variant c.551G>A p.(Gly184Asp), the primers
848 5'-CTGTCGAGGTGGATTCTAAAGC-3' (forward) and 5'-TGCATCCTTCTTTGCATCCT-3' (reverse) were
849 used.

850 **Analysis of the human sperm samples**

851 Human ejaculate samples from healthy donor and patient M2270, were analyzed according to WHO
852 guidelines prior to washing in buffer and centrifuged (1000 rpm, 20 min). The cells were fixed in
853 methanol and acetic acid (3:1) and used for immunofluorescence staining. Samples were dropped on
854 slides and permeabilized with 0.1% Triton x100. After blocking with 5% BSA for 30 min, slides were
855 incubated with primary CCIN or CYLC1 antibodies (concentrations shown in Table 3) for 3 h at room
856 temperature. Secondary antibodies were incubated for 1 h, followed by mounting with DAPI
857 containing medium. All stainings were repeated 3 times using aliquots of the same sample.

858 **Statistics**

859 For all analyses mean values +/- SD were calculated. Statistical significance was determined by One-
860 way ANNOVA analyses using Bonferroni correction. All experiments were conducted as biological
861 replicates and N is provided in Materials and methods section and/or figure legends.

862 **Materials and data availability statement:**

863 Custom made antibodies used in this study were developed against murine CYLC1 and CYLC2. A
864 limited amount of antibody can be provided upon request.

865 SpermQ software used for the analysis of the flagellar beat is publicly available
866 https://github.com/hansenjn/SpermQ .

867 For the purposes of this study a new code was written for color-coded figures and it's freely available
868 at https://github.com/hansenjn/ColorStackByTimeAndProject

869

870 **References**

871 1. Teves, M.E., Roldan, E.R.S., Krapf, D., Strauss, J.F., Bhagat, V., and Sapao, P. (2020). Sperm
872 Differentiation: The Role of Trafficking of Proteins. International journal of molecular sciences
873 *21*.

2. Longo, F.J., Krohne, G., and Franke, W.W. (1987). Basic proteins of the perinuclear theca of mammalian spermatozoa and spermatids: a novel class of cytoskeletal elements. The Journal of cell biology *105,* 1105–1120.
3. Longo, F.J., and Cook, S. (1991). Formation of the perinuclear theca in spermatozoa of diverse mammalian species: relationship of the manchette and multiple band polypeptides. Molecular reproduction and development *28,* 380–393.
4. Oko, R., and Sutovsky, P. (2009). Biogenesis of sperm perinuclear theca and its role in sperm functional competence and fertilization. Journal of reproductive immunology *83,* 2–7.
5. Oko, R., and Maravei, D. (1995). Distribution and possible role of perinuclear theca proteins during bovine spermiogenesis. Microscopy research and technique *32,* 520–532.
6. Zhang, M., Chiozzi, R.Z., Skerrett-Byrne, D.A., Veenendaal, T., Klumperman, J., Heck, A.J.R., Nixon, B., Helms, J.B., Gadella, B.M., and Bromfield, E.G. (2022). High Resolution Proteomic Analysis of Subcellular Fractionated Boar Spermatozoa Provides Comprehensive Insights Into Perinuclear Theca-Residing Proteins. Frontiers in cell and developmental biology *10,* 836208.
7. Zhang, X.-Z., Wei, L.-L., Jin, H.-J., Zhang, X.-H., and Chen, S.-R. (2022). The perinuclear theca protein Calicin helps shape the sperm head and maintain the nuclear structure in mice. Cell reports *40,* 111049.
8. Hamilton, L.E., Lion, M., Aguila, L., Suzuki, J., Acteau, G., Protopapas, N., Xu, W., Sutovsky, P., Baker, M., and Oko, R. (2021). Core Histones Are Constituents of the Perinuclear Theca of Murid Spermatozoa: An Assessment of Their Synthesis and Assembly during Spermiogenesis and Function after Gametic Fusion. International journal of molecular sciences *22*.
9. Sutovsky, P., Manandhar, G., Wu, A., and Oko, R. (2003). Interactions of sperm perinuclear theca with the oocyte: implications for oocyte activation, anti-polyspermy defense, and assisted reproduction. Microscopy research and technique *61,* 362–378.
10. Herrada, G., and Wolgemuth, D.J. (1997). The mouse transcription factor Stat4 is expressed in haploid male germ cells and is present in the perinuclear theca of spermatozoa. Journal of cell science *110 (Pt 14),* 1543–1553.
11. Tovich, P.R., and Oko, R.J. (2003). Somatic histones are components of the perinuclear theca in bovine spermatozoa. The Journal of biological chemistry *278,* 32431–32438.
12. Paranko, J., Longo, F., Potts, J., Krohne, G., and Franke, W.W. (1988). Widespread occurrence of calicin, a basic cytoskeletal protein of sperm cells, in diverse mammalian species. Differentiation; research in biological diversity *38,* 21–27.
13. Bülow, M. von, Heid, H., Hess, H., and Franke, W.W. (1995). Molecular nature of calicin, a major basic protein of the mammalian sperm head cytoskeleton. Experimental cell research *219,* 407–413.
14. Hess, H., Heid, H., and Franke, W.W. (1993). Molecular characterization of mammalian cylicin, a basic protein of the sperm head cytoskeleton. The Journal of cell biology *122,* 1043–1052.
15. Hess, H., Heid, H., Zimbelmann, R., and Franke, W.W. (1995). The protein complexity of the cytoskeleton of bovine and human sperm heads: the identification and characterization of cylicin II. Experimental cell research *218,* 174–182.
16. Bülow, M. von, Rackwitz, H.R., Zimbelmann, R., and Franke, W.W. (1997). CP beta3, a novel isoform of an actin-binding protein, is a component of the cytoskeletal calyx of the mammalian sperm head. Experimental cell research *233,* 216–224.
17. Hurst, S., Howes, E.A., Coadwell, J., and Jones, R. (1998). Expression of a testis-specific putative actin-capping protein associated with the developing acrosome during rat spermiogenesis. Molecular reproduction and development *49,* 81–91.
18. Tanaka, H., Yoshimura, Y., Nishina, Y., Nozaki, M., Nojima, H., and Nishimune, Y. (1994). Isolation and characterization of cDNA clones specifically expressed in testicular germ cells. FEBS Letters *355,* 4–10.

923 19. Heid, H., Figge, U., Winter, S., Kuhn, C., Zimbelmann, R., and Franke, W. (2002). Novel actin-
924 related proteins Arp-T1 and Arp-T2 as components of the cytoskeletal calyx of the mammalian
925 sperm head. Experimental cell research *279,* 177–187.
926 20. Rousseaux-Prévost, R., Lécuyer, C., Drobecq, H., Sergheraert, C., Dacheux, J.-L., and Rousseaux,
927 J. (2003). Characterization of boar sperm cytoskeletal cylicin II as an actin-binding protein.
928 Biochemical and biophysical research communications *303,* 182–189.
929 21. Wear, M.A., and Cooper, J.A. (2004). Capping protein: new insights into mechanism and
930 regulation. Trends in biochemical sciences *29,* 418–428.
931 22. Hansen, J.N., Rassmann, S., Jikeli, J.F., and Wachten, D. (2018). SpermQ¯A Simple Analysis
932 Software to Comprehensively Study Flagellar Beating and Sperm Steering. Cells *8*.
933 23. Gadadhar, S., Alvarez Viar, G., Hansen, J.N., an Gong, Kostarev, A., Ialy-Radio, C., Leboucher, S.,
934 Whitfield, M., Ziyyat, A., and Touré, A., et al. (2021). Tubulin glycylation controls axonemal
935 dynein activity, flagellar beat, and male fertility. Science (New York, N.Y.) *371*.
936 24. Okuda, H., DeBoer, K., O'Connor, A.E., Merriner, D.J., Jamsai, D., and O'Bryan, M.K. (2017).
937 LRGUK1 is part of a multiprotein complex required for manchette function and male fertility.
938 FASEB journal : official publication of the Federation of American Societies for Experimental
939 Biology *31,* 1141–1152.
940 25. Ng, P.C., and Henikoff, S. (2003). SIFT: Predicting amino acid changes that affect protein
941 function. Nucleic acids research *31,* 3812–3814.
942 26. Adzhubei, I.A., Schmidt, S., Peshkin, L., Ramensky, V.E., Gerasimova, A., Bork, P., Kondrashov,
943 A.S., and Sunyaev, S.R. (2010). A method and server for predicting damaging missense
944 mutations. Nature methods *7,* 248–249.
945 27. Richards, S., Aziz, N., Bale, S., Bick, D., Das, S., Gastier-Foster, J., Grody, W.W., Hegde, M., Lyon,
946 E., and Spector, E., et al. (2015). Standards and guidelines for the interpretation of sequence
947 variants: a joint consensus recommendation of the American College of Medical Genetics and
948 Genomics and the Association for Molecular Pathology. Genetics in medicine : official journal of
949 the American College of Medical Genetics *17,* 405–424.
950 28. World Health Organization (2021). WHO laboratory manual for the examination and processing
951 of human semen (Geneva).
952 29. Yoon, S.-Y., and Fissore, R.A. (2007). Release of phospholipase C zetaand Ca2+i oscillation-
953 inducing activity during mammalian fertilization. Reproduction (Cambridge, England) *134,* 695–
954 704.
955 30. Yoon, S.-Y., Jellerette, T., Salicioni, A.M., Lee, H.C., Yoo, M., Coward, K., Parrington, J., Grow, D.,
956 Cibelli, J.B., and Visconti, P.E., et al. (2008). Human sperm devoid of PLC, zeta 1 fail to induce
957 Ca(2+) release and are unable to initiate the first step of embryo development. The Journal of
958 Clinical Investigation *118,* 3671–3681.
959 31. Lécuyer, C., Dacheux, J.L., Hermand, E., Mazeman, E., Rousseaux, J., and Rousseaux-Prévost, R.
960 (2000). Actin-binding properties and colocalization with actin during spermiogenesis of
961 mammalian sperm calicin. Biology of reproduction *63,* 1801–1810.
962 32. Welch, J.E., and O'Rand, M.G. (1985). Identification and distribution of actin in spermatogenic
963 cells and spermatozoa of the rabbit. Developmental biology *109,* 411–417.
964 33. Russell, L.D., Weber, J.E., and Vogl, A. (1986). Characterization of filaments within the
965 subacrosomal space of rat spermatids during spermiogenesis. Tissue & cell *18,* 887–898.
966 34. Russell, L.D. (1979). Spermatid-Sertoli tubulobulbar complexes as devices for elimination of
967 cytoplasm from the head region late spermatids of the rat. The Anatomical record *194,* 233–
968 246.
969 35. Geyer, C.B., Inselman, A.L., Sunman, J.A., Bornstein, S., Handel, M.A., and Eddy, E.M. (2009). A
970 missense mutation in the Capza3 gene and disruption of F-actin organization in spermatids of
971 repro32 infertile male mice. Developmental biology *330,* 142–152.

36. Wear, M.A., Yamashita, A., Kim, K., Maéda, Y., and Cooper, J.A. (2003). How Capping Protein Binds the Barbed End of the Actin Filament. Current Biology *13,* 1531–1537.
37. Lehti, M.S., and Sironen, A. (2016). Formation and function of the manchette and flagellum during spermatogenesis. Reproduction (Cambridge, England) *151,* R43-54.
38. Mendoza-Lujambio, I., Burfeind, P., Dixkens, C., Meinhardt, A., Hoyer-Fender, S., Engel, W., and Neesen, J. (2002). The Hook1 gene is non-functional in the abnormal spermatozoon head shape (azh) mutant mouse. Human molecular genetics *11,* 1647–1658.
39. Hall, E.A., Keighren, M., Ford, M.J., Davey, T., Jarman, A.P., Smith, L.B., Jackson, I.J., and Mill, P. (2013). Acute versus chronic loss of mammalian Azi1/Cep131 results in distinct ciliary phenotypes. PLoS genetics *9,* e1003928.
40. Kierszenbaum, A.L., Rivkin, E., Tres, L.L., Yoder, B.K., Haycraft, C.J., Bornens, M., and Rios, R.M. (2011). GMAP210 and IFT88 are present in the spermatid golgi apparatus and participate in the development of the acrosome-acroplaxome complex, head-tail coupling apparatus and tail. Developmental dynamics : an official publication of the American Association of Anatomists *240,* 723–736.
41. Mochida, K., Tres, L.L., and Kierszenbaum, A.L. (1999). Structural and biochemical features of fractionated spermatid manchettes and sperm axonemes of theAzh/Azh mutant mouse. Molecular reproduction and development *52,* 434–444.
42. Courtot, A.M. (1991). Presence and localization of the 60 KD calicin in human spermatozoa presenting postacrosomal sheath defects: preliminary results. Molecular reproduction and development *28,* 272–279.
43. Wiel, L., Baakman, C., Gilissen, D., Veltman, J.A., Vriend, G., and Gilissen, C. (2019). MetaDome: Pathogenicity analysis of genetic variants through aggregation of homologous human protein domains. Human mutation *40,* 1030–1038.
44. Schneider, S., Balbach, M., Jan, F.J., Fietz, D., Nettersheim, D., Jostes, S., Schmidt, R., Kressin, M., Bergmann, M., and Wachten, D., et al. (2016). Re-visiting the Protamine-2 locus: deletion, but not haploinsufficiency, renders male mice infertile. Scientific reports *6,* 36764.
45. Truett, G.E., Heeger, P., Mynatt, R.L., Truett, A.A., Walker, J.A., and Warman, M.L. (2000). Preparation of PCR-quality mouse genomic DNA with hot sodium hydroxide and tris (HotSHOT). BioTechniques *29,* 52, 54.
46. Kotaja, N., Lin, H., Parvinen, M., and Sassone-Corsi, P. (2006). Interplay of PIWI/Argonaute protein MIWI and kinesin KIF17b in chromatoid bodies of male germ cells. Journal of cell science *119,* 2819–2825.
47. Schneider, S., Shakeri, F., Trötschel, C., Arévalo, L., Kruse, A., Buness, A., Poetsch, A., Steger, K., and Schorle, H. (2020). Protamine-2 Deficiency Initiates a Reactive Oxygen Species (ROS)-Mediated Destruction Cascade during Epididymal Sperm Maturation in Mice. Cells *9*.
48. Hughes, C.S., Moggridge, S., Müller, T., Sorensen, P.H., Morin, G.B., and Krijgsveld, J. (2019). Single-pot, solid-phase-enhanced sample preparation for proteomics experiments. Nature protocols *14,* 68–85.
49. Frankenfield, A.M., Ni, J., Ahmed, M., and Hao, L. (2022). Protein Contaminants Matter: Building Universal Protein Contaminant Libraries for DDA and DIA Proteomics. Journal of proteome research *21,* 2104–2113.
50. Käll, L., Storey, J.D., MacCoss, M.J., and Noble, W.S. (2008). Assigning significance to peptides identified by tandem mass spectrometry using decoy databases. Journal of proteome research *7,* 29–34.
51. Skinner, B.M., Rathje, C.C., Bacon, J., Johnson, E.E.P., Larson, E.L., Kopania, E.E.K., Good, J.M., Yousafzai, G., Affara, N.A., and Ellis, P.J.I. (2019). A high-throughput method for unbiased quantitation and categorization of nuclear morphology†. Biology of reproduction *100,* 1250–1260.

1021 52. Lüke, L., Tourmente, M., and Roldan, E.R.S. (2016). Sexual Selection of Protamine 1 in Mammals.
1022 Molecular biology and evolution *33,* 174–184.
1023 53. Yang, Z. (1997). PAML: a program package for phylogenetic analysis by maximum likelihood.
1024 Computer applications in the biosciences : CABIOS *13,* 555–556.
1025 54. Yang, Z. (2007). PAML 4: phylogenetic analysis by maximum likelihood. Molecular biology and
1026 evolution *24,* 1586–1591.
1027 55. Wyrwoll, M.J., Temel, Ş.G., Nagirnaja, L., Oud, M.S., Lopes, A.M., van der Heijden, G.W., Heald,
1028 J.S., Rotte, N., Wistuba, J., and Wöste, M., et al. (2020). Bi-allelic Mutations in M1AP Are a
1029 Frequent Cause of Meiotic Arrest and Severely Impaired Spermatogenesis Leading to Male
1030 Infertility. American journal of human genetics *107,* 342–351.
1031 56. Wyrwoll, M.J., Köckerling, N., Vockel, M., Dicke, A.-K., Rotte, N., Pohl, E., Emich, J., Wöste, M.,
1032 Ruckert, C., and Wabschke, R., et al. (2022). Genetic Architecture of Azoospermia-Time to
1033 Advance the Standard of Care. European urology.
1034

Figure 1

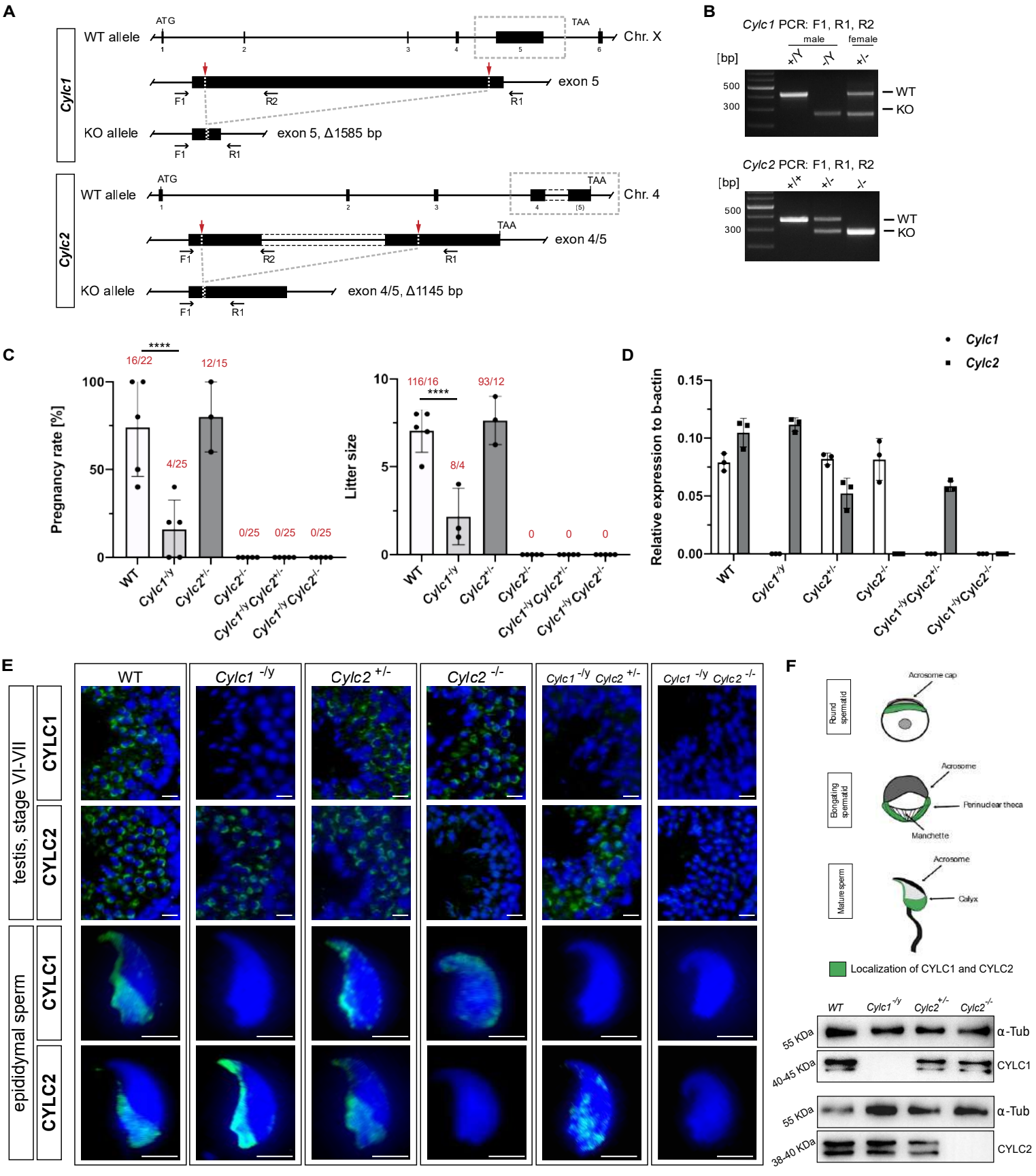
A
Cylc1
WT allele
ATG
TAA
Chr. X
exon 5
F1
R2
R1
KO allele
exon 5, Δ1585 bp
Cylc2
WT allele
Chr. 4
exon 4/5
KO allele
exon 4/5, Δ1145 bp
B
Cylc1 PCR: F1, R1, R2
male
female
[bp]
500
300
WT
KO
Cylc2 PCR: F1, R1, R2
C
Pregnancy rate [%]
Litter size
16/22
4/25
12/15
0/25
116/16
8/4
93/12
0
****
WT
Cylc1-/y
Cylc2+/-
Cylc2-/-
Cylc1-/yCylc2+/-
Cylc1-/yCylc2-/-
D
Cylc1
Cylc2
Relative expression to b-actin
E
testis, stage VI-VII
epididymal sperm
CYLC1
CYLC2
WT
Cylc1 -/y
Cylc2 +/-
Cylc2 -/-
Cylc1 -/y Cylc2 +/-
Cylc1 -/y Cylc2 -/-
F
Round spermatid
Acrosome cap
Elongating spermatid
Acrosome
Perinuclear theca
Manchette
Mature sperm
Calyx
Localization of CYLC1 and CYLC2
55 KDa
40-45 KDa
38-40 KDa
α-Tub
CYLC1
CYLC2

Figure 2

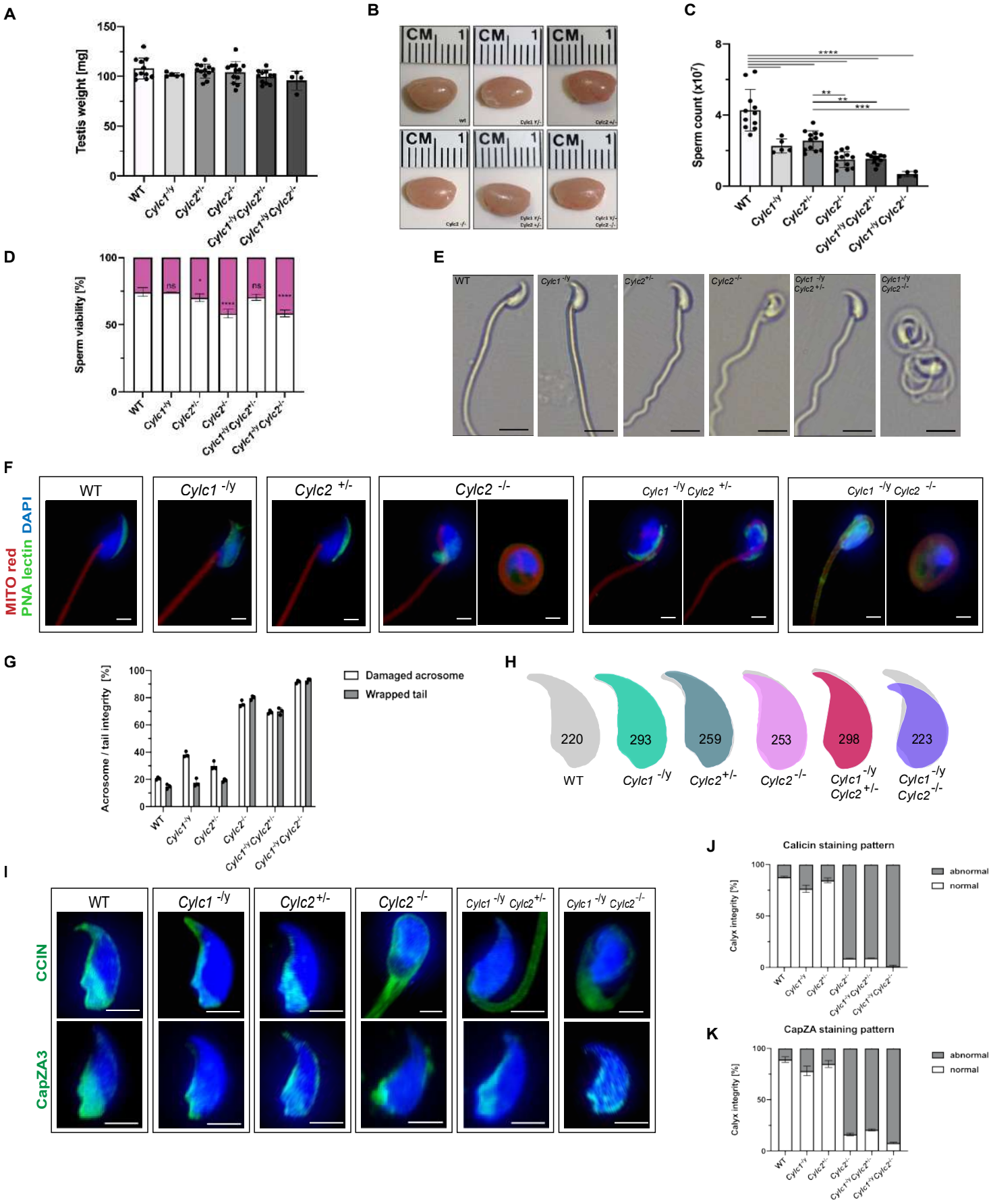
A
Testis weight [mg]
150
100
50
0
WT
Cylc1 -/y
Cylc2 +/-
Cylc2 -/-
Cylc1 -/y Cylc2 +/-
Cylc1 -/y Cylc2 -/-
B
CM 1
C
Sperm count (x10⁷)
8
4
0
****
**
**
***
D
Sperm viability [%]
100
50
0
ns
ns
E
WT
Cylc1 -/y
Cylc2 +/-
Cylc2 -/-
Cylc1 -/y Cylc2 +/-
Cylc1 -/y Cylc2 -/-
F
MITO red
PNA lectin
DAPI
WT
Cylc1 -/y
Cylc2 +/-
Cylc2 -/-
Cylc1 -/y Cylc2 +/-
Cylc1 -/y Cylc2 -/-
G
Acrosome / tail integrity [%]
100
80
60
40
20
0
Damaged acrosome
Wrapped tail
H
220
293
259
253
298
223
WT
Cylc1 -/y
Cylc2 +/-
Cylc2 -/-
Cylc1 -/y Cylc2 +/-
Cylc1 -/y Cylc2 -/-
I
CCIN
CapZA3
WT
Cylc1 -/y
Cylc2 +/-
Cylc2 -/-
Cylc1 -/y Cylc2 +/-
Cylc1 -/y Cylc2 -/-
J
Calicin staining pattern
Calyx integrity [%]
100
50
0
abnormal
normal
K
CapZA staining pattern
Calyx integrity [%]
100
50
0
abnormal
normal

Figure 3

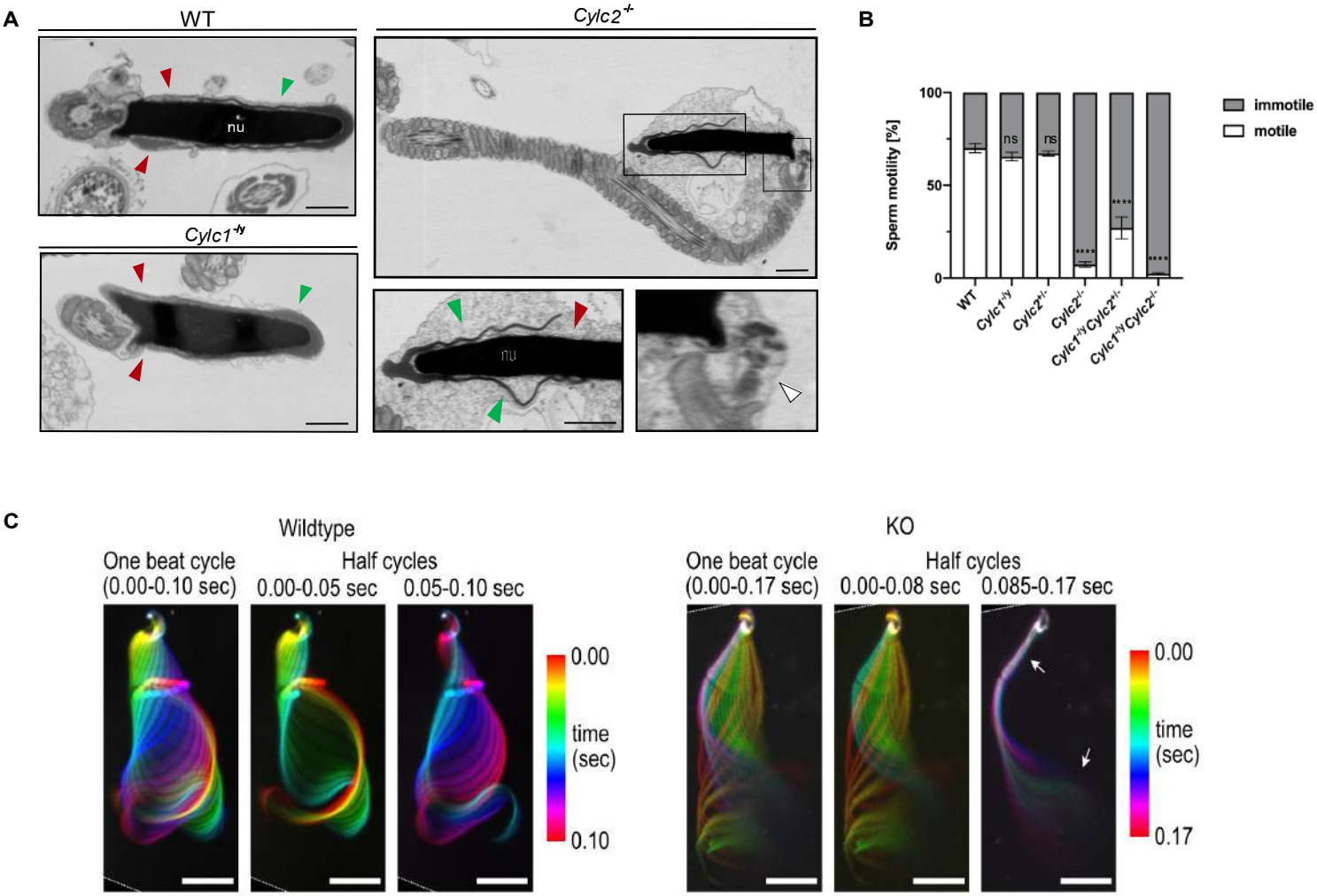
A
WT
nu
Cylc2-/-
Cylc1-/y
nu
B
Sperm motility [%]
100
50
0
ns
ns
****
****
****
immotile
motile
WT
Cylc1-/y
Cylc2+/-
Cylc2-/-
Cylc1-/yCylc2+/-
Cylc1-/yCylc2-/-
C
Wildtype
One beat cycle
(0.00-0.10 sec)
Half cycles
0.00-0.05 sec
0.05-0.10 sec
0.00
time
(sec)
0.10
KO
One beat cycle
(0.00-0.17 sec)
Half cycles
0.00-0.08 sec
0.085-0.17 sec
0.00
time
(sec)
0.17

Figure 4

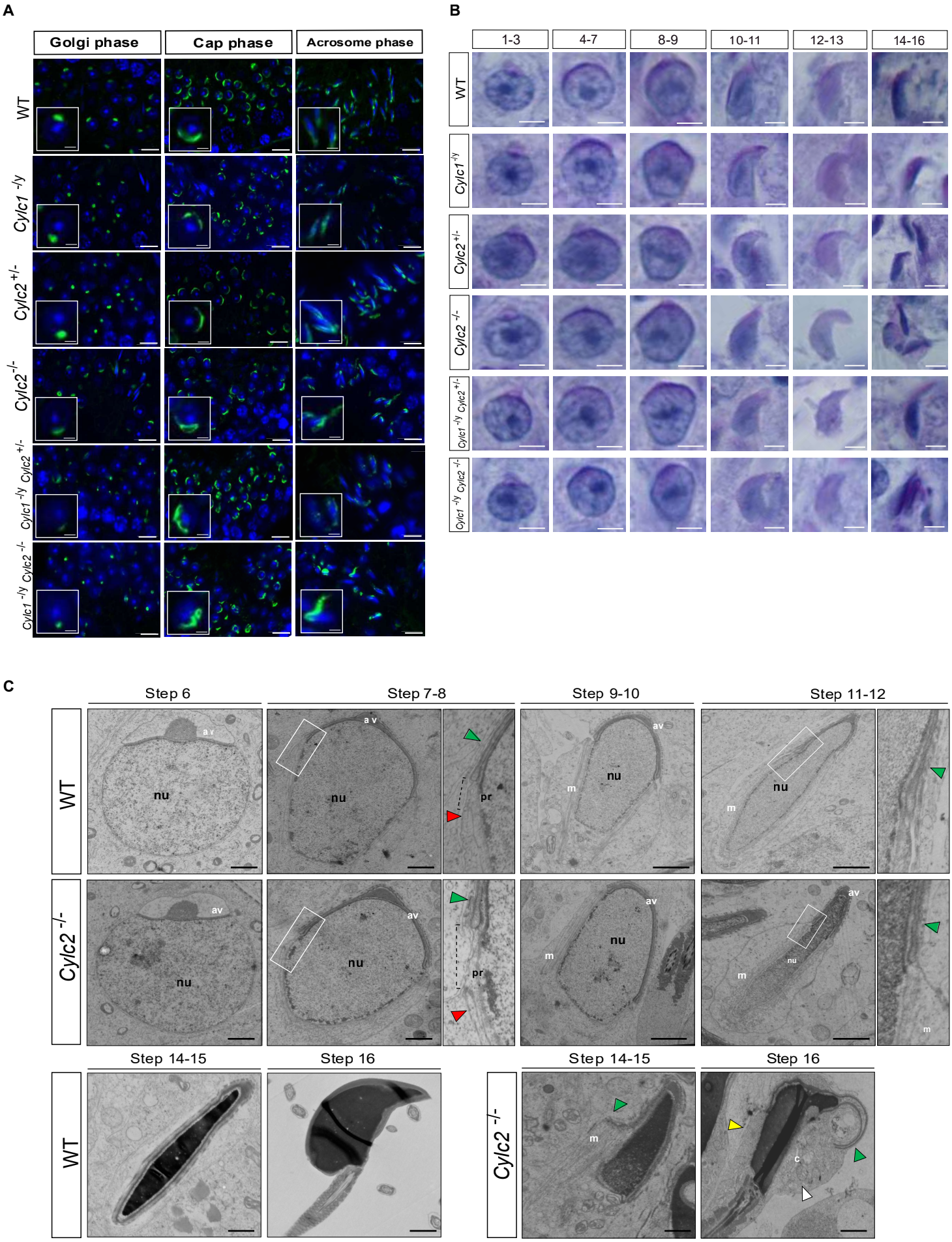
A
Golgi phase
Cap phase
Acrosome phase
WT
Cylc1 -/y
Cylc2 +/-
Cylc2 -/-
Cylc1 -/y Cylc2 +/-
Cylc1 -/y Cylc2 -/-
B
1-3
4-7
8-9
10-11
12-13
14-16
WT
Cylc1 -/y
Cylc2 +/-
Cylc2 -/-
Cylc1 -/y Cylc2 +/-
Cylc1 -/y Cylc2 -/-
C
Step 6
Step 7-8
Step 9-10
Step 11-12
WT
Cylc2 -/-
nu
av
pr
m
Step 14-15
Step 16
c

Figure 5

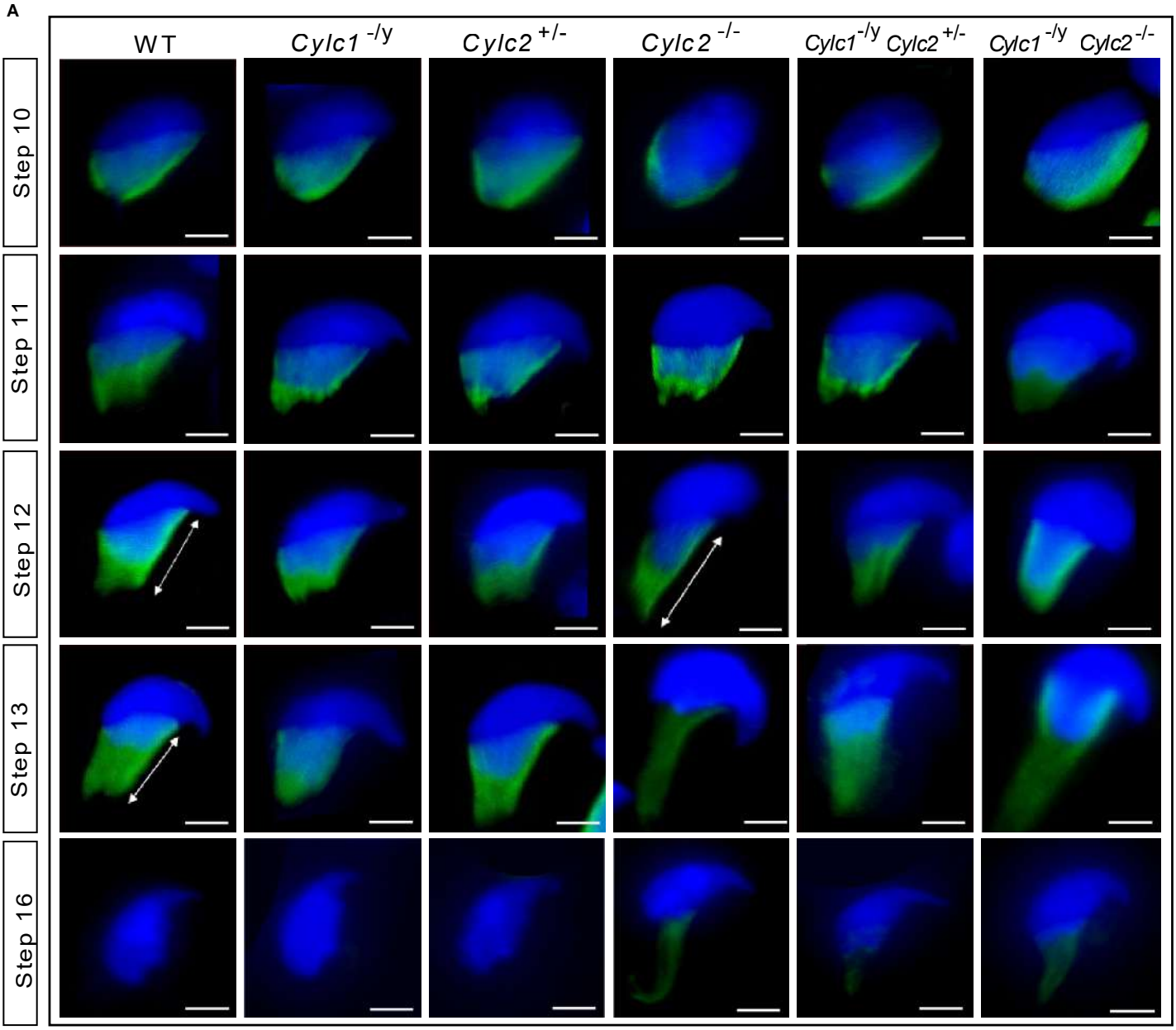
A
WT
Cylc1 -/y
Cylc2 +/-
Cylc2 -/-
Cylc1-/y Cylc2 +/-
Cylc1 -/y Cylc2 -/-
Step 10
Step 11
Step 12
Step 13
Step 16

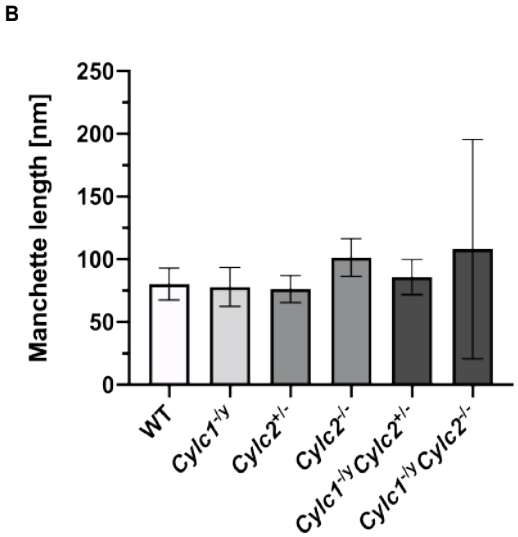
B
Manchette length [nm]
250
200
150
100
50
0
WT
Cylc1-/y
Cylc2+/-
Cylc2-/-
Cylc1-/y Cylc2+/-
Cylc1-/y Cylc2-/-

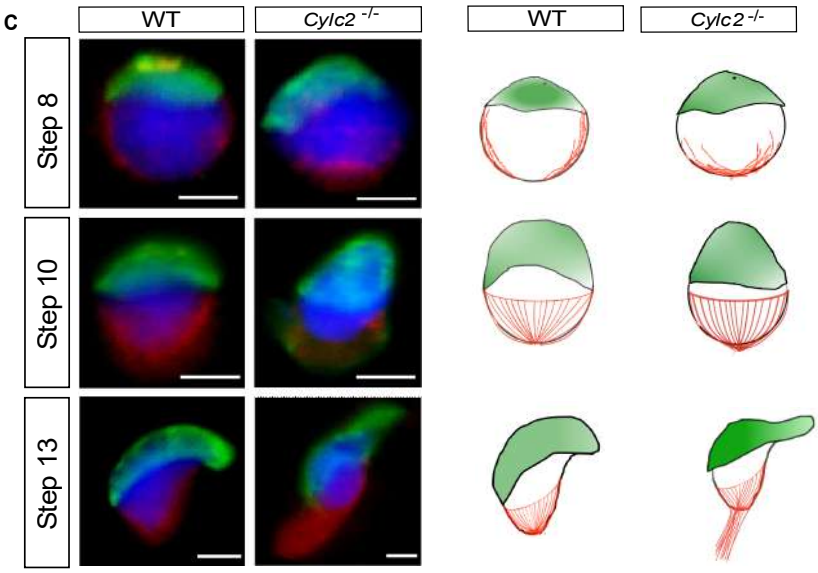
C
WT
Cylc2 -/-
WT
Cylc2 -/-
Step 8
Step 10
Step 13

Figure 6

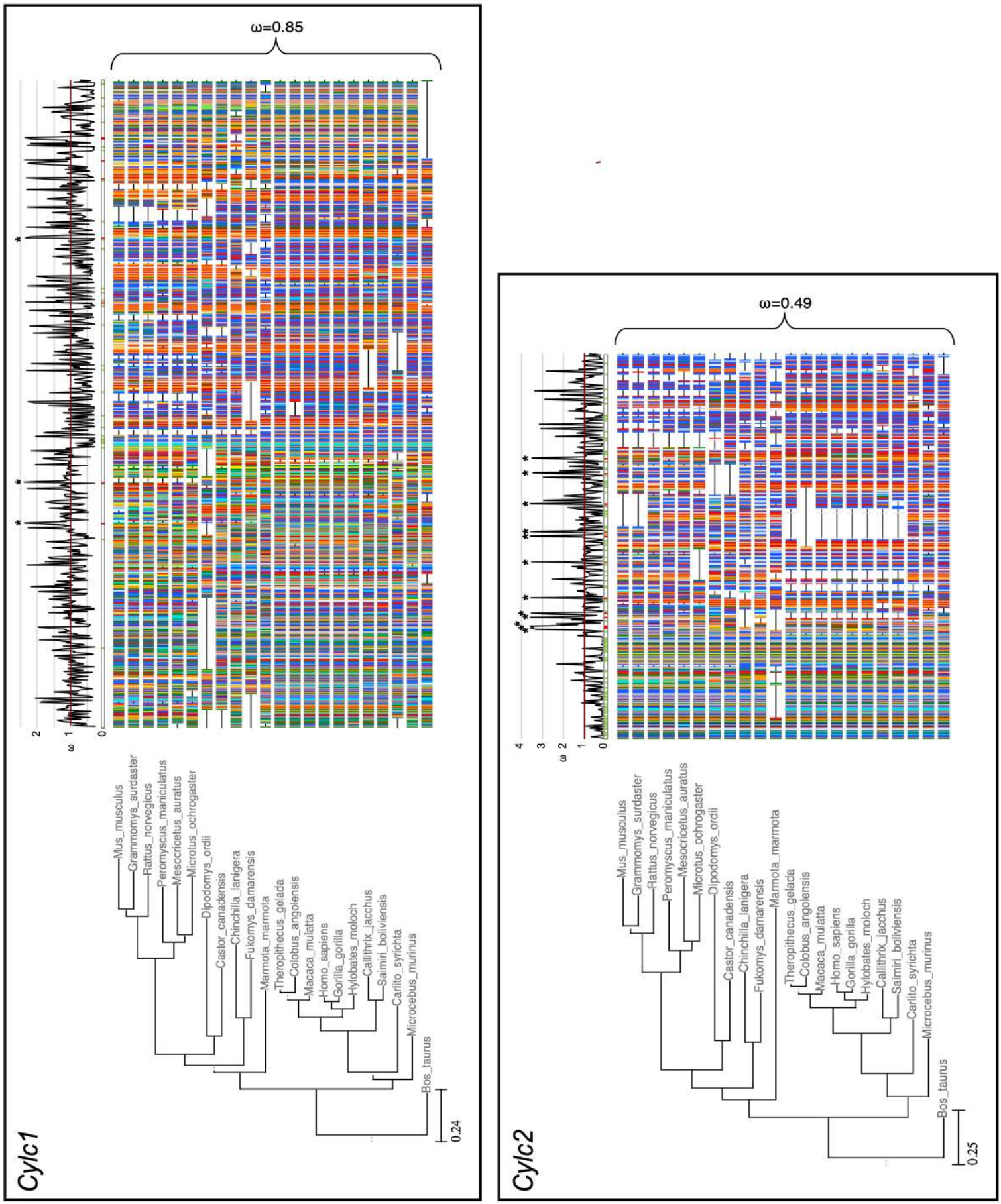
A
Cylc1
ω=0.85
ω 1
2
0
Mus_musculus
Grammomys_surdaster
Rattus_norvegicus
Peromyscus_maniculatus
Mesocricetus_auratus
Microtus_ochrogaster
Dipodomys_ordii
Castor_canadensis
Chinchilla_lanigera
Fukomys_damarensis
Marmota_marmota
Theropithecus_gelada
Colobus_angolensis
Macaca_mulatta
Homo_sapiens
Gorilla_gorilla
Hylobates_moloch
Callithrix_jacchus
Saimiri_boliviensis
Carlito_syrichta
Microcebus_murinus
Bos_taurus
0.24
B
Cylc2
ω=0.49
ω 2
4
3
1
0
Mus_musculus
Grammomys_surdaster
Rattus_norvegicus
Peromyscus_maniculatus
Mesocricetus_auratus
Microtus_ochrogaster
Dipodomys_ordii
Castor_canadensis
Chinchilla_lanigera
Fukomys_damarensis
Marmota_marmota
Theropithecus_gelada
Colobus_angolensis
Macaca_mulatta
Homo_sapiens
Gorilla_gorilla
Hylobates_moloch
Callithrix_jacchus
Saimiri_boliviensis
Carlito_syrichta
Microcebus_murinus
Bos_taurus
0.25

Figure 7

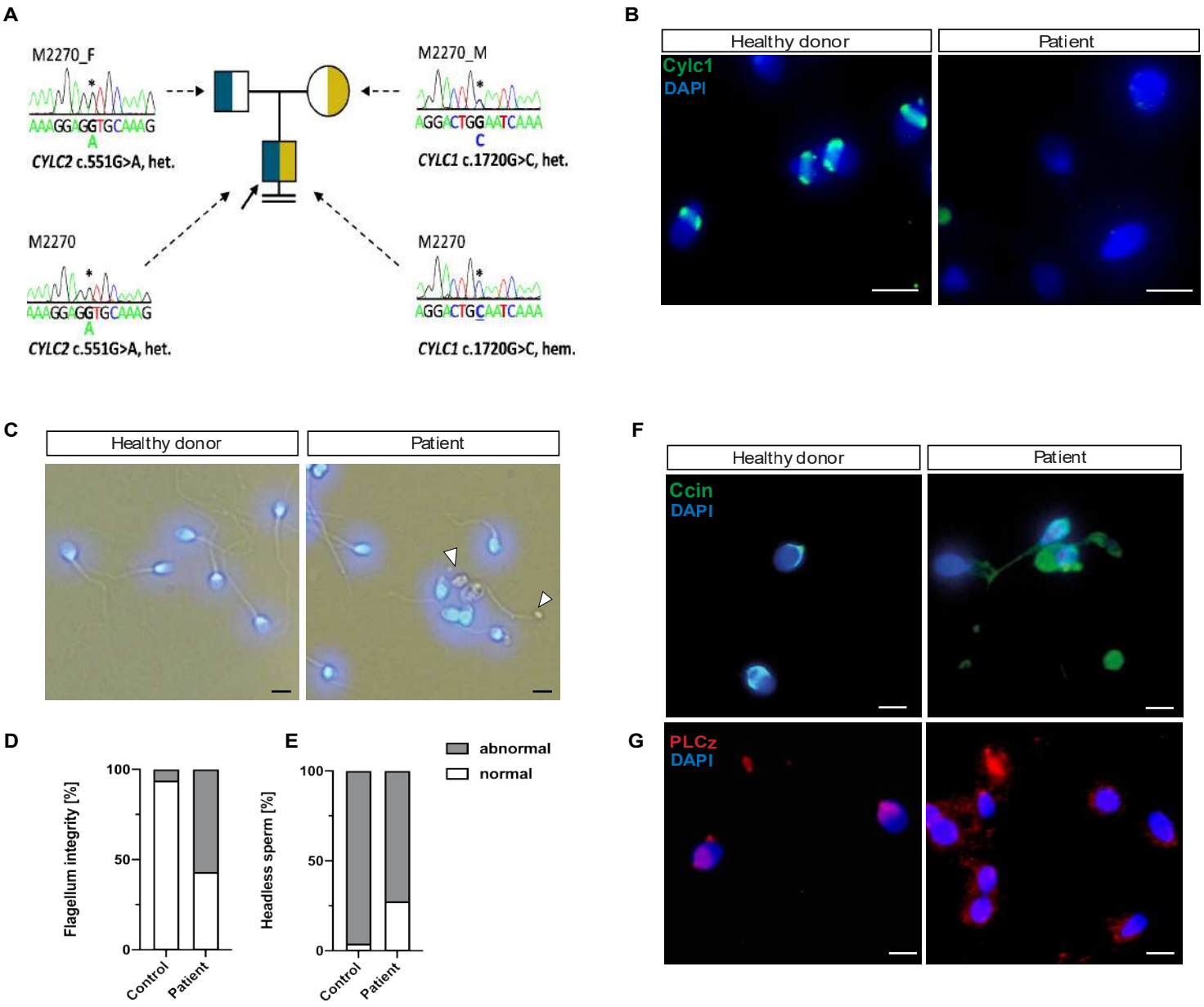
A
M2270_F
AAAGGAGGTGCAAAG
A
CYLC2 c.551G>A, het.
M2270_M
AGGACTGGAATCAAA
C
CYLC1 c.1720G>C, het.
M2270
AAAGGAGGTGCAAAG
A
CYLC2 c.551G>A, het.
M2270
AGGACTGCAATCAAA
CYLC1 c.1720G>C, hem.
B
Healthy donor
Patient
Cylc1
DAPI
C
Healthy donor
Patient
D
Flagellum integrity [%]
100
50
0
Control
Patient
E
Headless sperm [%]
100
50
0
Control
Patient
abnormal
normal
F
Healthy donor
Patient
Ccin
DAPI
G
PLCz
DAPI